Resource

Cell Chemical Biology

In Vitro and Cellular Probes to Study PARP Enzyme Target Engagement

Graphical Abstract

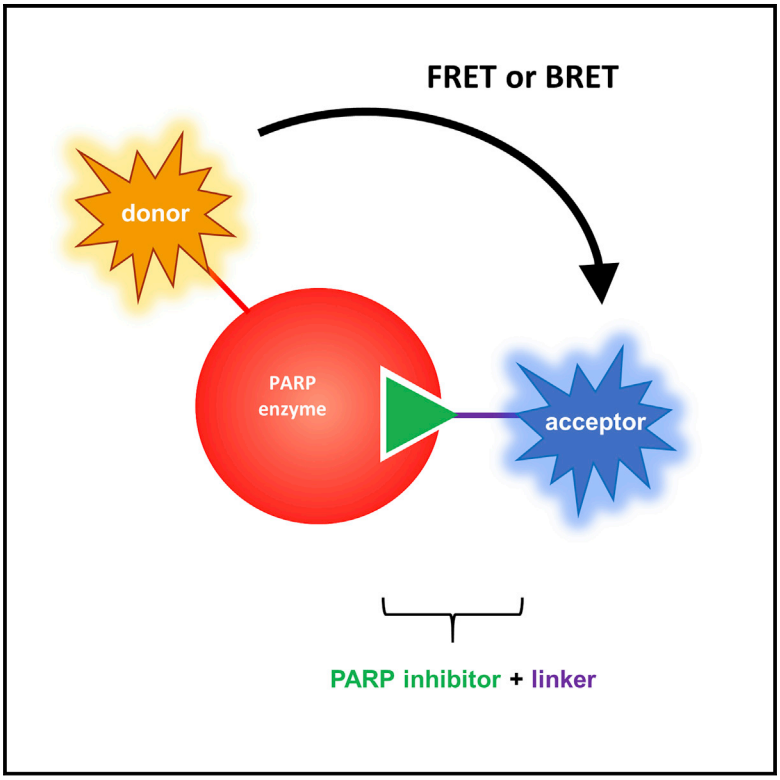

Authors

Tim J. Wigle, Danielle J. Blackwell, Laurie B. Schenkel, ..., Melissa M. Vasbinder, Heike Keilhack, Kevin W. Kuntz

Correspondence

twigle@ribontx.com

In Brief

Wigle et al. describe a versatile set of NAD^+-competitive probes for PARP enzymes that are used to build high-throughput *in vitro* and cellular biophysical assays that enable inhibitor screening and determination of residence time.

Highlights

- Exploited solvent-exposed region of PARP inhibitors to design NAD^+-competitive probes
- Probes used to develop assays for PARP enzymes that are agnostic of substrates
- TR-FRET assays are sensitive and discriminate high-potency inhibitors
- NanoBRET assays confirm cellular target engagement and measure residence time in cells

Wigle et al., 2020, Cell Chemical Biology *27*, 877–887
July 16, 2020
https://doi.org/10.1016/j.chembiol.2020.06.009

CellPress

Cell Chemical Biology

CellPress

Resource

In Vitro and Cellular Probes to Study PARP Enzyme Target Engagement

Tim J. Wigle,[1,2,*] Danielle J. Blackwell,[1] Laurie B. Schenkel,[1] Yue Ren,[1] W. David Church,[1] Hetvi J. Desai,[1] Kerren K. Swinger,[1] Andrew G. Santospago,[1] Christina R. Majer,[1] Alvin Z. Lu,[1] Mario Niepel,[1] Nicholas R. Perl,[1] Melissa M. Vasbinder,[1] Heike Keilhack,[1] and Kevin W. Kuntz[1]

[1]Ribon Therapeutics, 35 Cambridgepark Drive, Suite 300, Cambridge, MA 02140, USA

[2]Lead Contact

*Correspondence: twigle@ribontx.com

https://doi.org/10.1016/j.chembiol.2020.06.009

SUMMARY

Poly(ADP-ribose) polymerase (PARP) enzymes use nicotinamide adenine dinucleotide (NAD^+) to modify up to seven different amino acids with a single mono(ADP-ribose) unit (MARylation deposited by PARP monoenzymes) or branched poly(ADP-ribose) polymers (PARylation deposited by PARP polyenzymes). To enable the development of tool compounds for PARP monoenzymes and polyenzymes, we have developed active site probes for use in *in vitro* and cellular biophysical assays to characterize active site-directed inhibitors that compete for NAD^+ binding. These assays are agnostic of the protein substrate for each PARP, overcoming a general lack of knowledge around the substrates for these enzymes. The *in vitro* assays use less enzyme than previously described activity assays, enabling discrimination of inhibitor potencies in the single-digit nanomolar range, and the cell-based assays can differentiate compounds with sub-nanomolar potencies and measure inhibitor residence time in live cells.

INTRODUCTION

Human poly-ADP-ribose polymerase (PARP) enzymes are responsible for the mono(ADP-ribosylation) (MARylation deposited by PARP monoenzymes) and poly(ADP-ribosylation) (PARylation deposited by PARP polyenzymes) of serine, aspartic acid, glutamic acid, lysine, tyrosine, cysteine, and potentially arginine (Leutert et al., 2016). The protein family is sub-divided such that there are 12 enzymatically active PARP monoenzymes, 4 enzymatically active PARP polyenzymes, and 1 protein classified as catalytically inactive (PARP13). Both PARP monoenzymes and PARP polyenzymes utilize nicotinamide adenine dinucleotide (NAD^+) as the source of ADP-ribose (ADPr) and share similar active sites, where PARP polyenzymes have a conserved H-Y-E motif essential for catalysis and most PARP monoenzymes, with the exception of PARP3 and PARP4, have a conserved H-Y motif and an isoleucine, leucine, or tyrosine in place of the glutamate (Vyas et al., 2014).

The biological roles of the PARP polyenzymes are characterized to a greater extent than that of the monoenzymes. The PARP polyenzymes have been well explored with potent, selective small-molecule catalytic inhibitors (Thorsell et al., 2017) and PROTACs (Wang et al., 2019), and in the case of PARP1 and PARP2, approved drugs exist (olaparib, niraparib, rucaparib, and talazoparib). PARP monoenzymes play a role in the cellular stress response and are increasingly becoming linked to immunology, inflammation, and cancer (Butepage et al., 2015; Kunze and Hottiger, 2019; Vyas and Chang, 2014); however, there are only limited reports of PARP monoenzyme inhibitors that are suitable for interrogating these biological roles in cells or animal models. Of the PARP monoenzyme inhibitors that have been disclosed, potencies and intra-PARP family selectivity are modest and often the cellular target engagement is not confirmed by showing direct binding to the PARP or inhibition of the PARP's enzymatic activity (Carlile et al., 2016; Haikarainen et al., 2014a; Johannes et al., 2015; Lindgren et al., 2013; Morgan et al., 2019; Peng et al., 2017; Venkannagari et al., 2016; Yoneyama-Hirozane et al., 2017), with the exception of a potent PARP11-selective tool compound that inhibits auto-MARylation of PARP11 in 293 cells overexpressing the protein (Kirby et al., 2018).

Typically, a target-family approach to generating chemical probes relies on having biochemical and cell-based target engagement assays for multiple structurally and functionally related proteins. These assays enable the iterative medicinal chemistry design and testing cycles required to develop suitable selectivity and potency profiles in the inhibitors and to draw appropriate conclusions from cellular phenotypic studies. Previous biochemical screening for PARPs has been done using low-throughput biophysical methods (Wahlberg et al., 2012), DNA-encoded library screening (Yuen et al., 2019) or small-molecule microarray screening (Peng et al., 2017), which require establishment of complex chemistry, and enzyme assays that require high amounts of enzyme to generate a robust signal but limit the lower limit of potency resolution (Chen et al., 2018; Ji et al., 2018; Thorsell et al., 2017; Venkannagari et al., 2013; Wigle et al., 2019;

Yoneyama-Hirozane et al., 2017). The development of PARP monoenzyme assays is limited by a lack of understanding around the substrates for their MARylation activities, and at the time this work was initiated no antibodies capable of detecting MARylation existed. While substrate identification efforts for the PARP monoenzymes have been published (Carter-O'Connell et al., 2016; Carter-O'Connell et al., 2018; Feijs et al., 2013; Jwa and Chang, 2012; Lu et al., 2019; Yang et al., 2017), generating *in vitro* assays using the reported substrates has been challenging (Wigle et al., 2019).

During our efforts to develop NAD^+-competitive inhibitors of PARP monoenzymes we have developed an in-depth understanding of the structure-activity relationships (SAR) within the PARP family. We have identified regions of several NAD^+-competitive inhibitor templates that accommodate a wide range of substitutions without resulting in a loss of binding affinity. Inspired by previous work in the kinase field where pan-inhibitor templates have been used to generate *in vitro* fluorescent (Lebakken et al., 2007) and cellular NanoBRET probes (Machleidt et al., 2015), we took advantage of these observations and have generated a versatile set of NAD^+-competitive probes consisting of a PARP inhibitor connected to a fluorescent group or biotin moiety via a flexible linker. Here, we report the development of both *in vitro* and cellular probe displacement assays using these compounds. These high-throughput biophysical assays do not require knowledge of the substrate for each PARP, circumventing a challenge to screening these enzymes. The *in vitro* probe displacement assays are based on time-resolved fluorescence resonance energy transfer (TR-FRET) between acceptor and donor pairs bound to a hexahistidine (His6) tag on the protein and the biotin group on the active site probe. The TR-FRET assays correlate well to enzyme inhibition assays (Wigle et al., 2019), and use up to 50-fold less protein, typically improving the resolution of inhibitor potency to the single-digit nanomolar range. The cellular assays are based on bioluminescence resonance energy transfer (BRET) between a NanoLuc-tagged protein and a fluorescent group on the active site probe (NanoBRET). The NanoBRET assays typically resolve inhibitor potency into the triple-digit picomolar range. A series of PARP inhibitors was tested in both the TR-FRET and NanoBRET assays and we observed good correlation of potencies. In addition, we show that the NanoBRET assays can be used to investigate cellular residence times of PARP inhibitors. Overall, these assays are versatile biophysical tools that enable PARP chemical biology.

RESULTS

Design of TR-FRET and NanoBRET Probes

RBN010860 is an inhibitor originating from a fragment screening hit against PARP16 that binds to several H-Y-I/L/Y PARPs with sub-micromolar affinity as measured by surface plasmon resonance (SPR) (Figure 1E; Table S1). A crystal structure of RBN010860 bound to PARP16 is depicted in Figure 1A. PARP16 has a canonical three-dimensional structure of PARP monoenzyme active sites, and the binding mode of the compound in PARP16 is representative of the binding mode in other PARPs. The *cis* amide of the pyridazinone makes hydrogen bonds with the backbone of Gly153, and the aromatic ring stacks with Tyr193. In addition, the observed binding mode places the hydrophobic isoindoline group in a region where most PARP monoenzymes and polyenzymes are differentiated by the type of residue found in that position, with hydrophobic isoleucine, leucine, or tyrosine residues found in most monoenzymes (Leu189 and Tyr254 in PARP16), versus the polar glutamate found in polyenzymes, which contain the canonical H-Y-E motif (Glu1138 in PARP5b, Figure 1B). In addition to the energetic benefits of placing a hydrophobic group on the ligand near a hydrophobic residue in the protein, the isoindoline clashes with the glutamate in overlays with H-Y-E PARP crystal structures (not shown), further supporting the overall selectivity of this ligand for H-Y-I/L/Y PARPs over H-Y-E PARPs. It still retains binding to PARP1, PARP2 and PARP4, however on average relative to other H-Y-I/L/Y PARPs it is 17-, 13-, and 15-fold selective, respectively. In this PARP16 crystal structure, there are three independently solved copies of the protein-ligand complex per asymmetric unit, and when the three copies are superimposed, both the protein D loop and the piperidine moiety on the ligand reveal conformational flexibility. Notably, the piperidine in all three copies binds toward the surface of the pocket, exposing vectors that extend toward solvent. This observation was exploited in the design of TR-FRET (RBN011147) and NanoBRET (RBN011198) probes (Figure 1C). Extensions off the piperidine NH with linkers connected to either biotin or fluorophore NanoBRET 590SE led to probes that retained affinity to the H-Y-I/L/Y PARPs when compared with the parent molecule, RBN010860. Based on the published crystal structure of the literature inhibitor PJ34 bound to PARP5b (Figure 1B) (Abdelkarim et al., 2001; Haikarainen et al., 2014b), a separate probe was designed for the H-Y-E PARPs, which includes the monoenzymes, PARP3 and PARP4. Using a similar concept, and exploiting a solvent-exposed vector, linkers connected to the fluorophore NanoBRET 590SE were extended off the parent molecule RBN011829, an analog of PJ34, to yield RBN012148 (Figure 1D). The affinities of the probes for all the PARP enzymes are shown in Figure 1E and tabulated in Table S1.

Development of TR-FRET Probe Displacement Assays for H-Y-I/L/Y PARPs Using RBN011147

The binding of RBN011147 to H-Y-(I/L/Y) PARPs was confirmed using TR-FRET where donor/acceptor pairs consisting of two configurations shown in Figure 2A were examined: (1) streptavidin labeled with europium chelate + anti-His antibody labeled with ULight dye and (2) streptavidin labeled with ULight dye + anti-His antibody labeled with europium chelate. The configuration that gave the best signal-to-background for each PARP was identified and selected for further assay development. An example of the assay development process followed is shown for PARP7 in Figures 2B–2E. First, a simultaneous titration of enzyme, active site probe, donor, and acceptor was performed and conditions for further assay development were selected based on achieving concentrations near the apex of the hook points while minimizing protein use and ensuring robust signal-to-background (Figure 2B). DMSO titrations were performed to understand the sensitivity of the binding signal to the solvent used for solubilizing the test compounds (Figure 2C). In many instances there was significant DMSO sensitivity above 1% and we chose to use 0.25% DMSO in the assays to avoid major loss of signal. To search for control compounds for each assay, a reference set of PARP inhibitors plus the parent compound of the probe (RBN010860) was

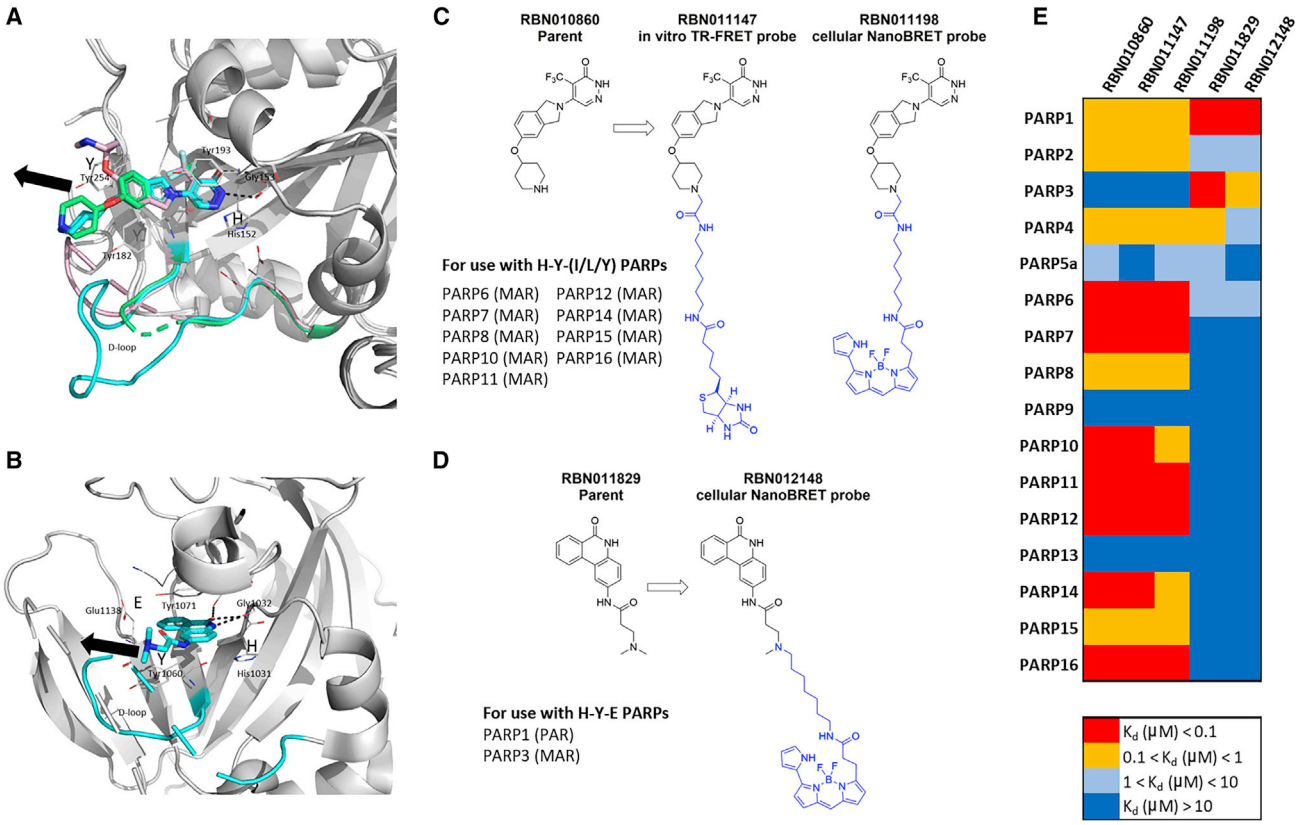

Figure 1. Development of NAD$^+$-Competitive Probes for PARP Enzymes

(A) Crystal structure of RBN010860 bound to PARP16 at 2.1 Å. Three independently solved copies of the protein-ligand complex from the asymmetric unit are superimposed. Protein is depicted as a gray cartoon. The protein D loop, a flexible loop near the active site found in structures of all PARPs that have been structurally characterized, is colored cyan, green, and pink in the three different chains. RBN010860 is displayed in sticks and is colored to match the protein chain to which it is bound.

(B) The crystal structure of PARP5b bound to PJ34 (PDB: 4BJB) is similarly depicted. The D loop and inhibitor are colored cyan. Black arrows show the solvent-exposed vectors that were exploited for both types of probes.

(C) The pan-H-Y-(I/L/Y) PARP inhibitor RBN010860 was derivatized with a linker plus biotin or NanoBRET 590SE, respectively yielding the TR-FRET probe RBN011147 and the NanoBRET probe RBN011198 for H-Y-(I/L/Y) PARP assay development. The type of ADP-ribosylation deposited by each enzyme is denoted in parentheses.

(D) The potent PARP1 and PARP3 inhibitor RBN011829 was derivatized with a linker plus NanoBRET 590SE, yielding the NanoBRET probe RBN012148 for PARP1 and PARP3 assay development. The type of ADP-ribosylation deposited by each enzyme is denoted in parentheses.

(E) The binding affinities of the parent molecules and probes were measured using SPR.

screened in dose-response format (Figure 2D). Finally, the assay was transferred to automated liquid handling dispensing equipment and the uniformity of test plates containing vehicle or fully blocked active site by RBN010860 were performed and the reproducibility was judged using the *Z′* factor (Zhang et al., 1999). This process was repeated for all H-Y-I/L/Y PARP enzymes, and final assay conditions are summarized in Table S3 and correlation of TR-FRET probe displacement half-maximal inhibitory concentration (IC_{50}) values to enzyme inhibition values calculated using the self-modification enzyme assay (Wigle et al., 2019) are shown in Figure 3.

Development of NanoBRET Probe Displacement Assays for H-Y-I/L/Y and H-Y-E PARPs Using RBN011198 and RBN012148

The general scheme for the NanoBRET assays is shown in Figure 4A. RBN011198 was used to develop a NanoBRET assay for several H-Y-I/L/Y PARPs (an example is shown for PARP7 in Figure 4), and RBN012148 was used to develop NanoBRET assays for PARP1 and PARP3 (an example for PARP3 is shown in Figure 5). Transient expression of PARP enzymes fused to a NanoLuc tag on the N or C terminus was tested in 293T cells (Figure 4B for PARP7, Figure 5A for PARP3). Constructs that showed a luminescence signal greater than 100-fold above the empty vector control were deemed sufficient for assay development and were then tested for binding to the probe, and the K_d for this interaction was calculated (Figures 4C and 5B). The construct with the best assay window was chosen for assay development, with preference often given to full-length constructs to better represent the physiologically relevant form of the enzyme, and we moved forward setting the probe concentration to equal its K_d value. To search for appropriate control compounds, the parent of the probe as well as a reference set of PARP inhibitors were screened in a dose-response format

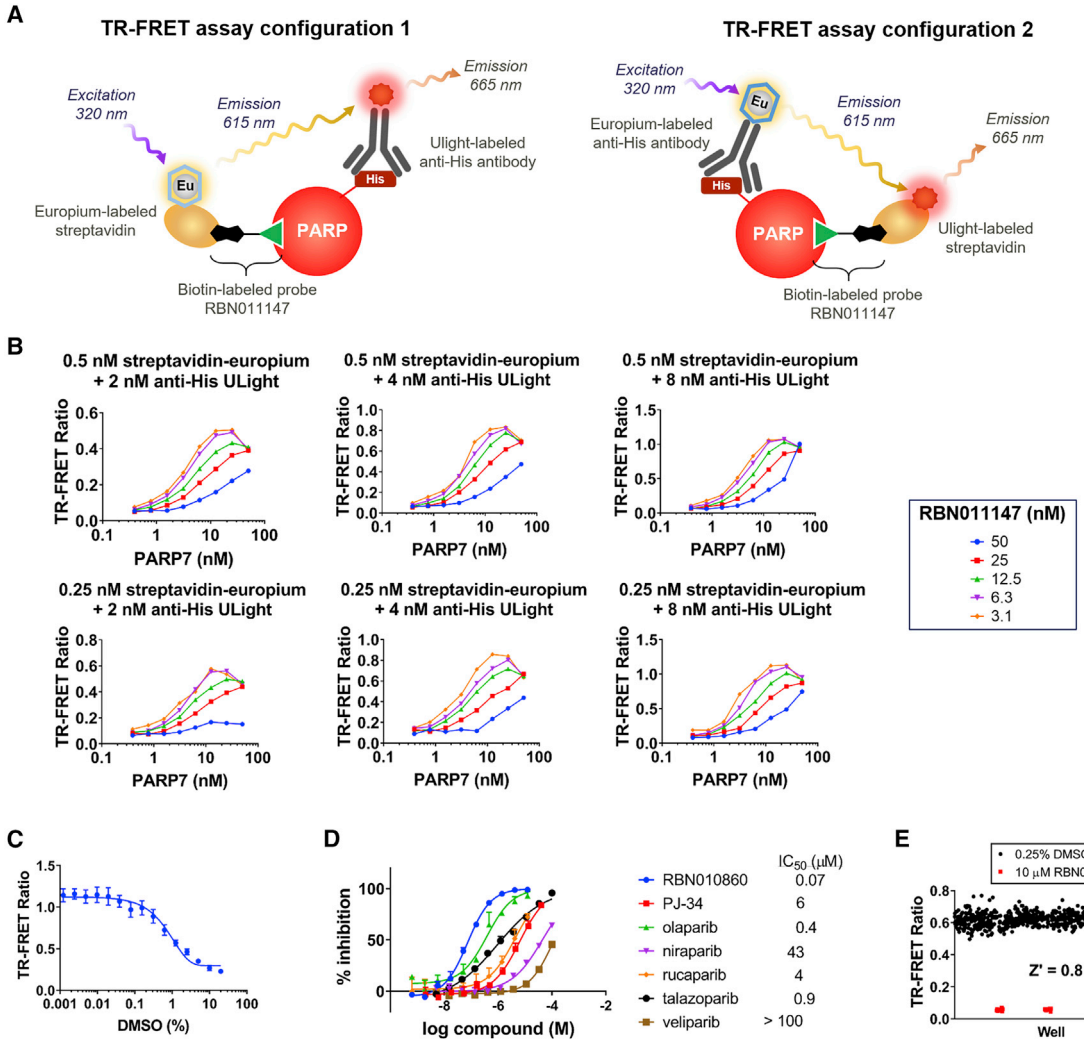

Figure 2. PARP7 Probe Displacement Assay Development Using TR-FRET

(A) Configuration 1 of the TR-FRET assay with streptavidin-labeled europium (donor) and ULight-labeled anti-His6 antibody (acceptor) is shown on the left, while configuration 2 of the TR-FRET assay with europium-labeled anti-His6 antibody (donor) and ULight-labeled streptavidin (acceptor) is shown on the right.

(B) Simultaneous titration of PARP7, RBN011147, and donor/acceptor pairs was performed to select conditions leading to the most robust assay.

(C) DMSO titrations showed the assay is sensitive (IC_{50} = 0.9%) to the solvent used for the compounds. Data are represented as mean ± SEM.

(D) A reference set of compounds, including the active site probe parent compound (RBN010860) and literature PARP1 inhibitors screened to identify a compound to be used as a positive control. Data are represented as mean ± SEM.

(E) Uniformity of the fully automated assay is tested to ensure robust and reproducible performance.

(Figures 4D and 5C). The assays were then automated using liquid handling equipment and the uniformity of test plates containing vehicle or fully blocked active site was assessed using the *Z′* factor (Zhang et al., 1999) (Figures 4E and 5D). Final assay conditions and constructs used for each assay are shown in Tables S4 and S5 and correlation of TR-FRET and NanoBRET probe displacement IC_{50} values are shown in Figure 6.

Measurement of PARP7 and PARP14 Inhibitor Binding Kinetics in Cells Using NanoBRET

We used the NanoBRET concept to assess the residence times of PARP7 and PARP14 inhibitors of varying degrees of potency and compared them with residence time measurements performed using SPR. The NanoBRET residence time measurement was performed by incubating 293T cells overexpressing NanoLuc-PARP fusion proteins with the test inhibitor at 10-fold its measured IC_{50} value. Following compound treatment, the excess unbound inhibitor was removed using multiple rapid washing steps and the cells were resuspended in medium containing the NanoBRET probe at 10-fold its K_d value. By observing the NanoBRET signal increase as a function of time we inferred the rate at which the inhibitor was dissociating from the PARP and being replaced by the NanoBRET probe (overall scheme for experiment shown in Figure 7A). For PARP7, RBN010860 is a fast-off inhibitor in both SPR ($t_{1/2}$ = 18 s) and NanoBRET (<60 s), while RBN012337 has a very long residence time in SPR (216 min) and NanoBRET (too slow to measure in this format) (Figures 7B–7D). For PARP14, RBN010860 is a fast-off inhibitor

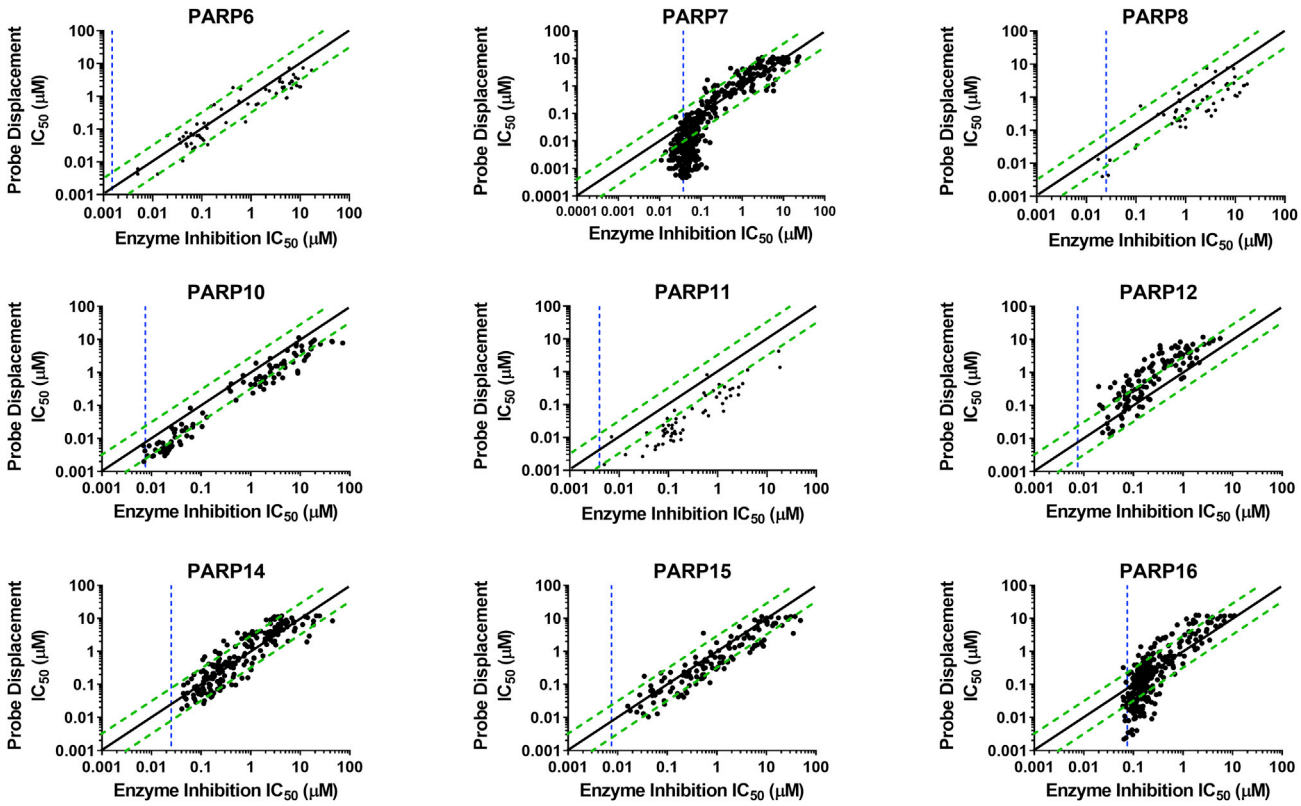

Figure 3. Correlation of TR-FRET Probe Displacement Assay and Enzyme Inhibition Assay

Dose responses of PARP inhibitors were tested using *in vitro* probe displacement TR-FRET assays and *in vitro* enzyme inhibition assays (Wigle et al., 2019). Solid black lines represent a 1:1 correlation and dashed green lines represent 3:1 and 1:3 correlations. The vertical blue dashed lines represent the theoretical potency limit of the enzyme inhibition assays, equivalent to half of the enzyme concentration.

in both SPR ($t_{1/2}$ = 32 s) and NanoBRET (<60 s), while RBN013293 has a modest residence time in SPR (19 min) and NanoBRET (12 min) (Figures 7E and 7F). The structures of RBN012337 and RBN013293 are shown in Figure S1.

DISCUSSION

The limited knowledge around the identity of PARP substrates renders development of enzyme activity assays suitable for the discovery and characterization of potent and selective small molecules challenging, particularly among the PARP monoenzyme subfamily, which for all but PARP3 and PARP4 contain a catalytic triad of H-Y-I/L/Y residues. We have previously used a family-wide approach to developing *in vitro* enzyme activity assays that relies upon immobilizing the enzymes on a microplate surface to induce molecular crowding, forcing the enzymes to self-modify (Wigle et al., 2019). We have used these assays to generate SAR for a series of PARP inhibitors; however, the high enzyme concentrations needed to observe robust signal in many cases limits the ability to discriminate between potent inhibitors. In addition, there are no MAR-selective antibodies available for use in cell-based assay development to understand cellular target engagement, although very recently an antibody recognizing both MAR and PAR has been characterized (Lu et al., 2019).

In this study we exploited our knowledge of the SAR for multiple series of NAD^+-competitive PARP inhibitors to design a set of derivatized small-molecule probes that bind in the NAD^+-binding site of most PARP enzymes. We used these probes to develop a series of sensitive *in vitro* and cellular biophysical assays that rely upon detecting the displacement of the probes from the enzyme using TR-FRET or NanoBRET, respectively. The pan-monoenzyme inhibitor RBN010860 served as the starting point for design of the monoenzyme active site probes. Functionalization of the piperidine nitrogen, which provides a vector to access the solvent-exposed region of the protein, enabled incorporation of many different substitutions while retaining potency (the full SAR for this template will be described in a future publication). Derivatizing RBN010860 using this vector with a linker connected to a biotin group led to the TR-FRET probe (RBN011147), and when linked to the fluorophore NanoBRET 590SE led to the NanoBRET probe (RBN011198). Both probe molecules RBN011147 and RBN011198 retained binding affinity to nearly all H-Y-I/L/Y PARPs similar to the parent molecule RBN010860, and enabled the development of TR-FRET assays for PARP6, PARP7, PARP8, PARP10, PARP11, PARP12, PARP14, PARP15, and PARP16, and NanoBRET assays for PARP7, PARP10, PARP11, PARP12, PARP14, and PARP16. While the TR-FRET format worked for all enzymes tested, we note that we were unable to generate NanoBRET assays for

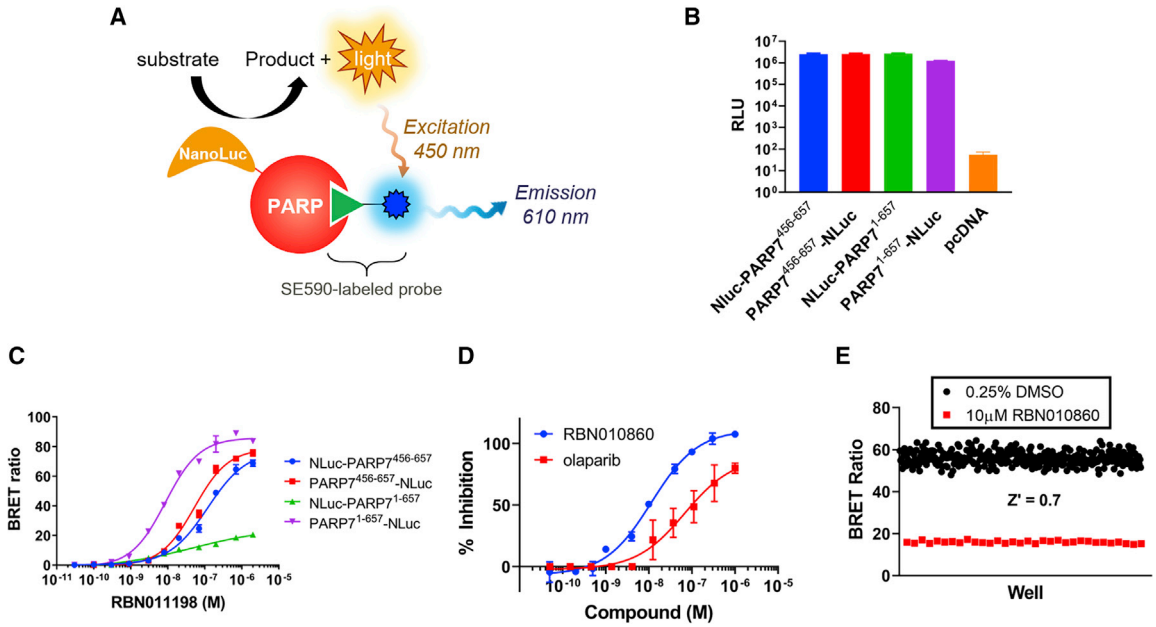

Figure 4. PARP7 Probe Displacement Assay Development Using NanoBRET

(A) Configuration of the NanoBRET assay where a NanoLug-tagged PARP enzyme generates light from the NanoLuc substrate, which in turn excites the NanoBRET 590SE dye in the probe, causing an emission of light with a wavelength of 610 nm.

(B) The expression of catalytic domain (amino acids 456–657) or full-length PARP7 (amino acids 1–657) with N- and C-terminal NanoLuc fusions was investigated in 293T cells. An empty vector control transfection (pcDNA) was performed to assess the background signal. Data are represented as mean ± SEM.

(C) Titration of the probe RBN011198 was performed against all constructs that were expressed inside the 293T cells. K_d^{app} values were as follows Nluc-PARP7$^{456-657}$ = 100 nM, PARP7$^{456-657}$-Nluc = 50 nM, Nluc-PARP7$^{1-657}$ = 50 nM, and PARP7$^{1-657}$-Nluc = 10 nM. Data are represented as mean ± SEM.

(D) Control inhibitors were tested for the displacement of RBN011198 in 293T cells under final assay conditions. Data are represented as mean ± SEM.

(E) The uniformity of the final assay was tested in 384-well format and the *Z′* was 0.7.

PARP6, PARP8, and PARP15. Previous efforts have shown that pan-H-Y-E PARP inhibitors could be used to generate active site probes for fluorescence polarization (Papeo et al., 2014). We derivatized a similar parent molecule (RBN011829) with the fluorophore NanoBRET 590SE to generate the probe RBN012148, which extends the concept of probe displacement for H-Y-E PARPs into the cellular milieu through the development of NanoBRET assays for PARP1 and PARP3.

To understand whether probe displacement correlated with inhibition of enzymatic activity, a collection of NAD^+-competitive PARP inhibitors was tested in dose-response format in both the TR-FRET assay and a previously described enzymatic assay measuring self-modification of immobilized PARP enzymes (Wigle et al., 2019). The IC_{50} values generated in each assay typically fall within 3-fold of each other, indicating that the TR-FRET probe displacement assay is a good surrogate for enzyme inhibition when characterizing NAD^+-competitive inhibitors (Figure 3) and the IC_{50} for NAD^+ was in-line with its K_M value (data not shown). In many instances, the TR-FRET assays use a much lower concentration of enzyme compared with the self-modification assay (Table S6). The high amounts of PARP protein required to observe a signal in the self-modification assays limits the ability to discriminate potent inhibitors since the lowest IC_{50} value measurable is equivalent to half the protein concentration used (Copeland, 2005). This is evident in the case of the PARP7 and PARP16, which use 75 and 150 nM protein, respectively, in the enzyme activity assay compared with 3 nM of each protein in the probe displacement assay. For these enzymes, the TR-FRET assay discriminates compounds over roughly 1–2 more logs of potency as evidenced by the "hockey stick" shape of those correlation plots. In addition, the lower concentration of protein used in the TR-FRET assay combined with the reduced assay volume results in a much lower consumption of protein when screening inhibitors. There have been reports that inhibitors of the DNA-binding PARPs (PARP1, PARP2, and PARP3) may have potency underestimated when assessed in enzyme assays using truncated constructs (Thorsell et al., 2017). We investigated if this effect occurred for PARP14, an H-Y-I/L-Y PARP, and compared the potency of a series of inhibitors against full-length and truncated PARP14 comprised of only the catalytic domain, and did not observe a shift in potency (Figure S2).

We further compared IC_{50} data generated in the biochemical assays (either TR-FRET probe displacement or self-modification enzyme inhibition) to the NanoBRET assays (Figure 6). While the constructs are overexpressed as NanoLuc fusions, which may impact their subcellular localization, we note that overall the cell-based data correlate with the *in vitro* data. The PARP1 and PARP14 biochemical to NanoBRET potency correlation plots did contain some outliers, with compounds being less potent in the NanoBRET assay. In the case of PARP14, many outliers had low permeability ($P_{app\ (A-B)}$ <3 × 10^{-6} cm/s) in an MDCK-MDR1 assay, which may contribute to their shift in cellular potency. It has been established that PARP1 trapping onto DNA may account for the mechanism of action of some chemotypes

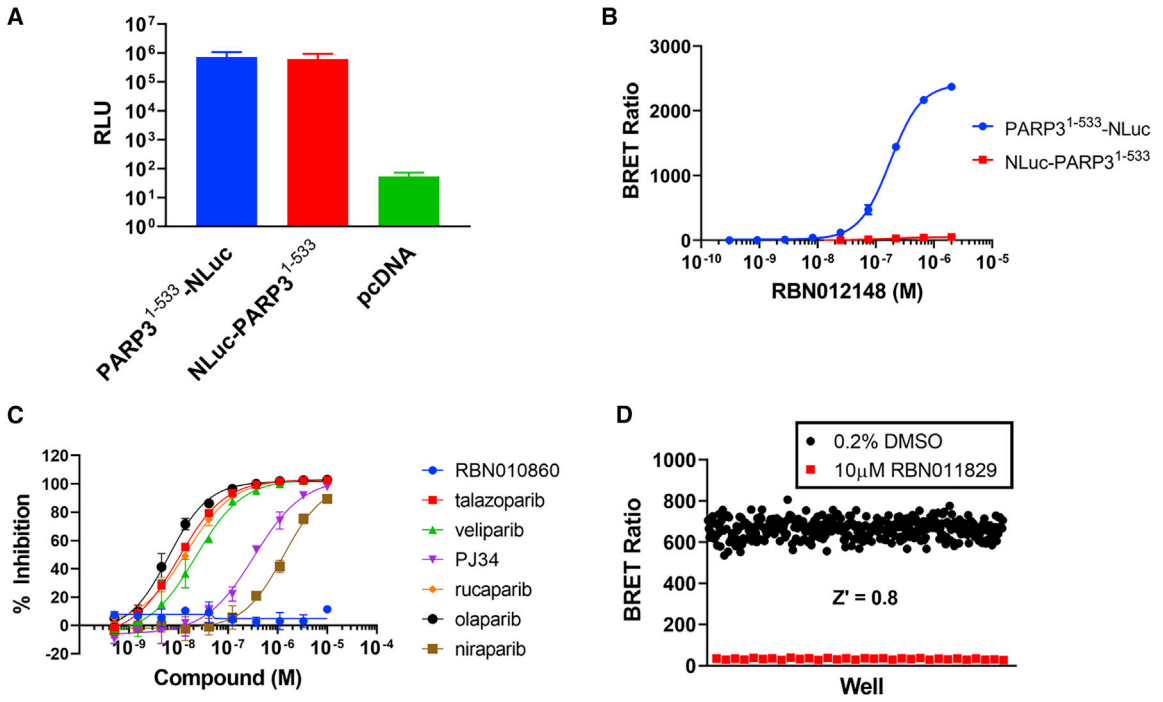

Figure 5. PARP3 Probe Displacement Assay Development Using NanoBRET

(A) The expression of full-length PARP3 (amino acids 1–533) with N- and C-terminal NanoLuc fusions was investigated in 293T cells. An empty vector control transfection (pcDNA) was performed to assess the background signal. Data are represented as mean ± SEM.

(B) Titration of the probe RBN012148 was performed against all constructs that were expressed inside the 293T cells. The measured K_d values were: $PARP3^{1-533}$ NLuc = 176 nM and NLuc-$PARP3^{1-533}$ = 167 nM. Data are represented as mean ± SEM.

(C) Control inhibitors were tested for the displacement of RBN012148 in 293T cells under final assay conditions. Data are represented as mean ± SEM.

(D) The uniformity of the final assay was tested in 384-well format and the *Z′* was 0.8.

of PARP1 inhibitors (Murai et al., 2012; Wang et al., 2019), and the biochemical enzyme inhibition assay used here for PARP1 contains DNA to activate the enzyme. It is possible that the NanoBRET assay measures the binding to the apo protein, and the enzyme inhibition assay is measuring the PARP1 trapping potency of the inhibitor versus a PARP1-DNA complex. In addition, we included a reported PARP11 cell-active tool compound (Kirby et al., 2018) in this study and observed that it had IC_{50} = 28 nM in the PARP11 enzyme inhibition assay and IC_{50} = 61 nM in the PARP11 NanoBRET assay. It had modest activity for PARP7, 10, and 14 in both assays but was at least 10-fold selective for PARP11 over those enzymes.

It is becoming increasingly apparent that understanding an inhibitor's residence time on a target is important throughout the drug discovery process. Often, in the early stages of drug discovery there is a desire to be able to screen compounds with reasonable throughput to assess residence time to understand structure-kinetic relationships, and in the later stages to understand *in vivo* pharmacologic outcomes (Copeland, 2016). Traditionally the ability to do this has mainly been limited to *in vitro* techniques (Copeland et al., 2011; Renaud et al., 2016). Recently, NanoBRET probe displacement has been applied to other target classes to understand residence time in the complex cellular milieu where proteins may exist in complexes, have diverse post-translational modifications, and are interacting with substrates whose concentrations may be fluctuating (Bouzo-Lorenzo et al., 2019; Ong et al., 2020; Robers et al., 2015). We used slow-off and fast-off inhibitors of PARP7 and PARP14 to show that cellular residence time can be measured for the PARP enzymes using NanoBRET and that, for these enzyme-inhibitor pairs, the residence time measured by SPR aligns closely with the NanoBRET value. This technique has sufficient throughput to screen multiple compounds in parallel in one experiment and will be useful to inform medicinal chemistry design. In addition, the understanding of cellular residence time will help build the relationship between exposure and pharmacodynamic and phenotypic effects when testing PARP inhibitors *in vivo*.

SIGNIFICANCE

ADP-ribosylation is an important post-translational modification involved in the cellular stress response and has been linked to immunology, inflammation and cancer. The poly(ADP-ribose) polymerase (PARP) family are the major human enzymes responsible for the deposition of ADP-ribose. There are 16 enzymatically active members among the 17 proteins in the PARP family, and while all of them use nicotinamide adenine dinucleotide (NAD^+) to ADP-ribosylate their substrates, they can be further sub-divided based on key residues in their active site and the type of modification they perform. PARP polyenzymes typically have a catalytic triad of H-Y-E in their active site and deposit long, branched polymers of poly(ADP-ribose), while mono-enzymes typically have a catalytic triad of H-Y-I/L/Y and

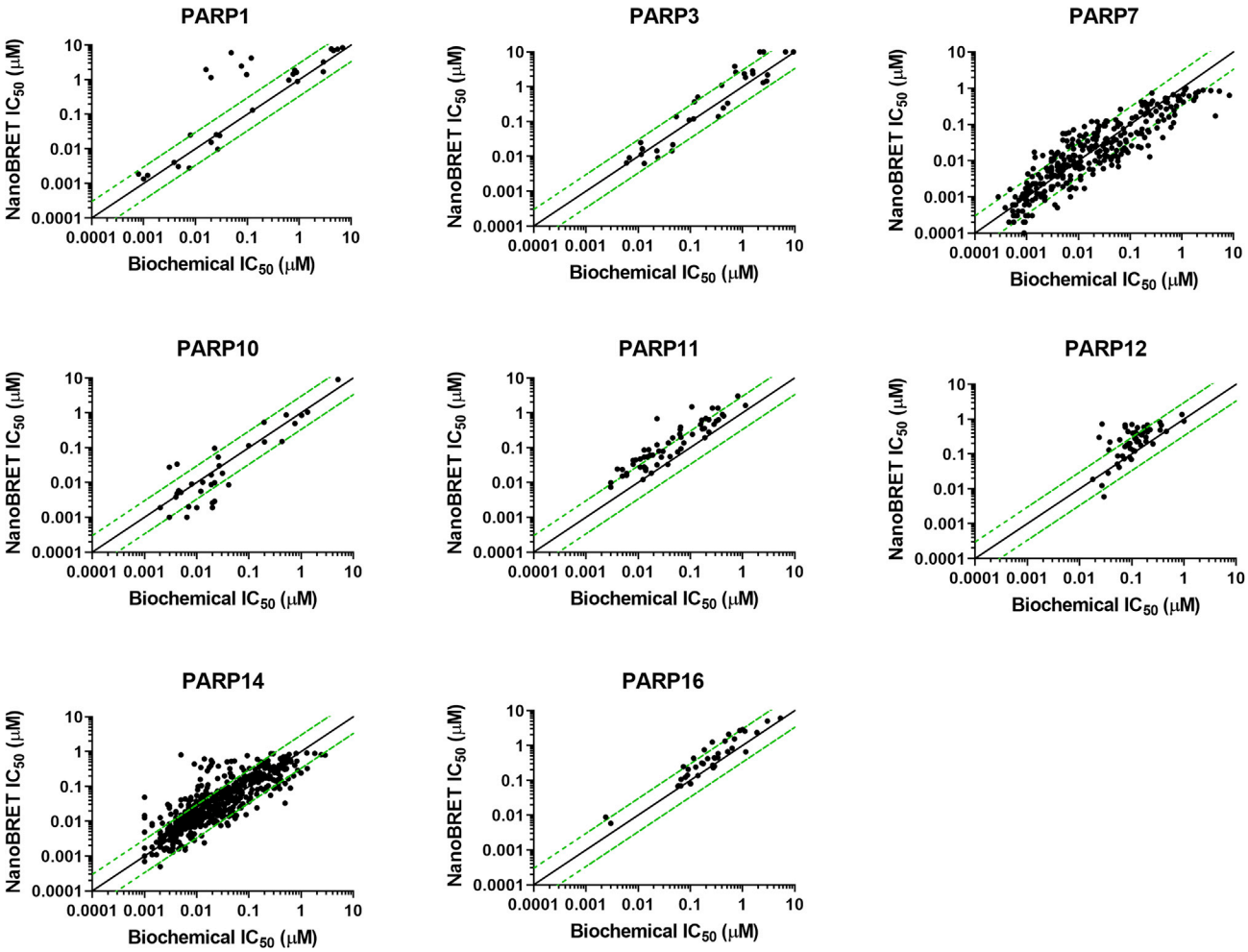

Figure 6. Correlation of NanoBRET Cellular Probe Displacement and Biochemical Assays

Dose responses of PARP inhibitors were tested using NanoBRET assays and biochemical TR-FRET probe displacement or enzyme inhibition assays (Wigle et al., 2019). Solid black lines represent a 1:1 correlation and dashed green lines represent 3:1 and 1:3 correlations.

deposit a single mono(ADP-ribose). While the biological role of poly(ADP-ribosylation) has been extensively studied with small-molecule inhibitors, far less is known about mono(-ADP-ribosylation). A major challenge to developing assays for the PARP monoenzymes is the lack of knowledge around how they engage their substrates. To enable the discovery and development of inhibitors for H-Y-I/L/Y PARPs, we designed NAD$^+$-competitive probe molecules for *in vitro* and cellular biophysical probe displacement assays. Using these probes, we developed TR-FRET assays for PARP6, PARP7, PARP8, PARP10, PARP11, PARP12, PARP14, PARP15, and PARP16, and NanoBRET assays for PARP7, PARP10, PARP11, PARP12, PARP14, and PARP16. In addition, we disclose an NAD$^+$-competitive probe for H-Y-E PARPs and develop NanoBRET assays for PARP1 and PARP3. These probe displacement assays are agnostic of the substrates for the PARP enzymes, are highly sensitive and correlate well with each other, as well as with the inhibition of enzymatic activity. Overall, they are high-throughput methods that will enable hit finding, lead optimization, and inform on cellular target engagement for PARP inhibitors to enable a family-wide approach to chemical biology.

STAR★METHODS

Detailed methods are provided in the online version of this paper and include the following:

- KEY RESOURCES TABLE
- RESOURCE AVAILABILITY
  - Lead Contact
  - Materials Availability
  - Data Code and Availability
- EXPERIMENTAL MODEL AND SUBJECT DETAILS
  - Cell Lines
- METHOD DETAILS
  - Recombinant Protein Production
  - TR-FRET Probe Displacement Assays
  - NanoBRET Probe Displacement Assays
  - Cellular Binding Kinetics

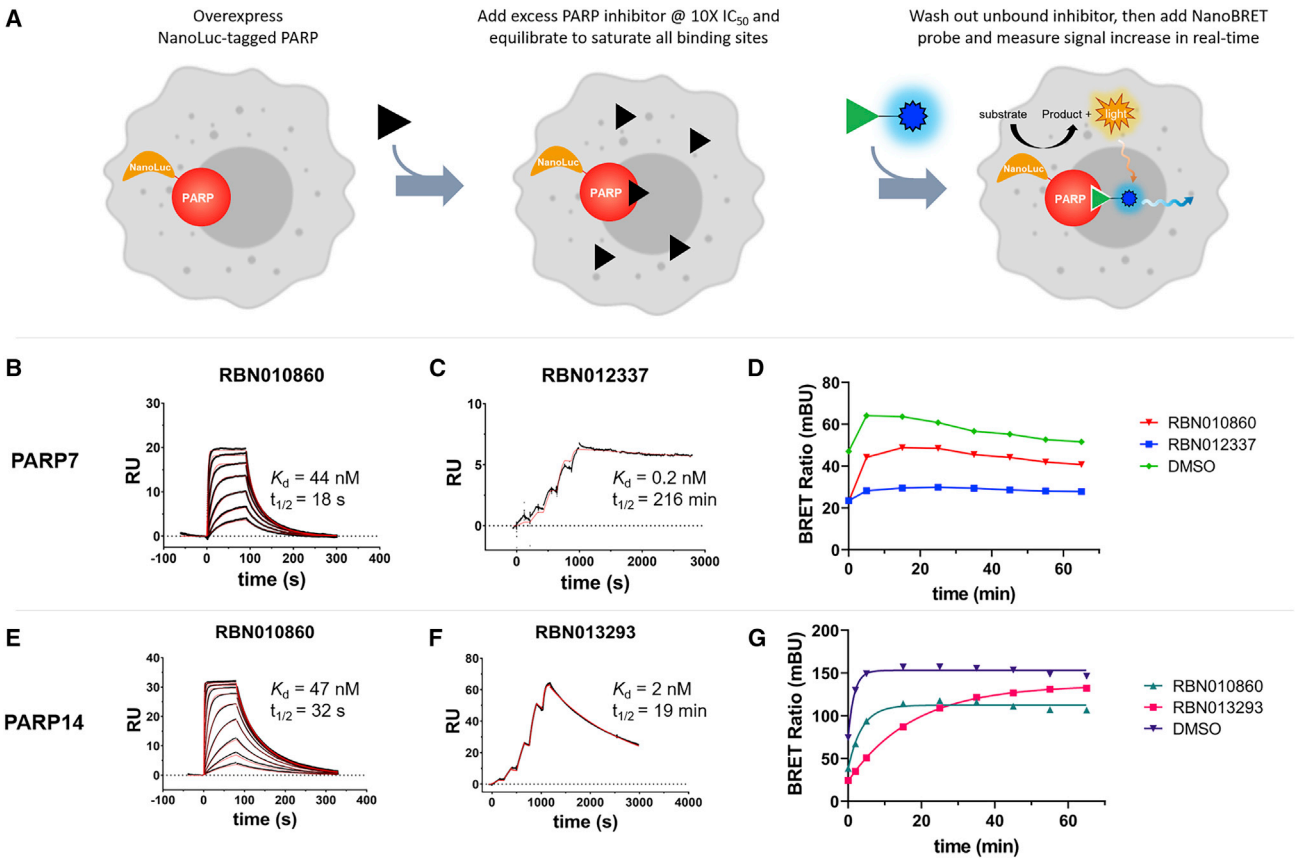

Figure 7. Measuring Cellular Residence Time Using NanoBRET Probe Displacement Assay

(A) Scheme for testing residence time in cells using the NanoBRET assay.

(B) SPR sensorgrams from single, discreet injections of RBN010860 against PARP7 was fit using kinetic binding models and the affinity and half-life are indicated.

(C) Single-cycle kinetic SPR binding data for RBN012337 against PARP7 was fit using kinetic binding models, and the affinity and half-life are indicated.

(D) RBN010860 is a fast-off inhibitor of PARP7 in cells, while RBN012337 is an extremely slow-off inhibitors for which a half-life value could not be fit on the timescale of the experiment.

(E) SPR sensorgrams from single, discreet injections of RBN010860 against PARP14 was fit using kinetic binding models and the affinity and half-life are indicated. (F) Single-cycle kinetic SPR binding data for RBN013293 against PARP14 was fit using kinetic binding models, and the affinity and half-life are indicated.

(G) RBN010860 is a fast-off inhibitor of PARP14 in cells (half-life < 1 min), while RBN013293 is a modestly slow-off inhibitor (half-life = 12 min). Data were fit using a one-phase exponential association model.

- Self-Modification Enzyme Assays
- Surface Plasmon Resonance (SPR)
- X-Ray Crystallography
- General Chemical Synthesis
- Synthesis of 5-[5-(Piperidin-4-yloxy)-2,3-dihydro-1*H*-isoindol-2-yl]-4-(trifluoromethyl)-2,3-dihydropyridazin-3-one (RBN010860)
- Synthesis of 5-[(3aS,4S,6aR)-2-Oxo-hexahydro-1*H*-thieno[3,4-d]imidazolidin-4-yl]-*N*-(6-[2-[4-([2-[6-oxo-5-(trifluoromethyl)-1,6-dihydropyridazin-4-yl]-2,3-dihydro-1*H*-isoindol-5-yl]oxy)piperidin-1-yl]acetamido] hexyl)pentanamide (RBN011147)
- Synthesis of 3-(5,5-difluoro-7-(1H-pyrrol-2-yl)-5H-5l4,6l4-dipyrrolo[1,2-c:2',1'-f][1,3,2]diazaborinin-3-yl)-N-(6-(2-(4-((2-(6-oxo-5-(trifluoromethyl)-1,6-dihydropyridazin-4-yl)isoindolin-5-yl)oxy)piperidin-1-yl)acetamido)hexyl)propanamide (RBN011198)
- Synthesis of 3-(dimethylamino)-N-(6-oxo-5,6-dihydrophenanthridin-2-yl)propenamide (RBN011829)
- Synthesis of 3-(5,5-difluoro-7-(1H-pyrrol-2-yl)-5H-5λ^4,6λ^4-dipyrrolo[1,2-c:2',1'-f][1,3,2]diazaborinin-3-yl)-N-(6-(methyl(3-oxo-3-((6-oxo-5,6-dihydrophenanthridin-2-yl)amino)propyl)amino)hexyl)propenamide (RBN012148)

- QUANTIFICATION AND STATISICAL ANALYSIS
  - Data Analysis for In Vitro Active Site Probe Displacement TR-FRET Assays
  - Data Analysis for Cellular Active Site Probe Displacement NanoBRET Assays
  - % Inhibition
  - IC_{50} Curve Fitting
  - Pass/Fail Criteria for Screening Plates

SUPPLEMENTAL INFORMATION

Supplemental Information can be found online at https://doi.org/10.1016/j.chembiol.2020.06.009.

ACKNOWLEDGMENTS

We would like to thank Mr. Matt Robers at Promega for technical guidance during assay development and Dr. Victoria Richon for helpful discussions in the preparation of this manuscript. In addition, we thank Ms. Ping Wei and her team at Viva Biotech for plasmid generation, protein production, and X-ray crystallography, Dr. Hara Black and her team at Evotec SE for protein production, Dr. Dennis Wegener and his team at Evotec SE for surface plasmon resonance studies, Dr. Po-wai Yuen and Dr. Cheng Shao and their team at Pharmaron, and Dr. Anthony Cuzzupe and his team at SYNthesis for synthesis of the compounds and probes. We thank Mr. Chris Reik at Ribon Therapeutics for technical assistance with the PARP3 NanoBRET experiments. This work was funded by Ribon Therapeutics.

AUTHOR CONTRIBUTIONS

M.M.V., L.B.S., and K.K.S. designed the active site probes. K.K.S. oversaw X-ray crystallography and T.J.W. oversaw the surface plasmon resonance. M.M.V., L.B.S., and N.R.P. oversaw synthesis of all compounds. T.J.W., W.D.C., and C.R.M. developed *in vitro* probe displacement assays and D.J.B., Y.R., and H.J.D. developed the cellular probe displacement assays. A.G.S. ran assays and plated compounds. D.J.B., Y.R., and A.Z.L. developed the MAR ICW assays. T.J.W. conceived and designed the experiments and T.J.W., K.W.K., H.K., and M.N. supervised the work. T.J.W. wrote the manuscript with contributions from D.J.B., K.K.S., M.M.V., and L.B.S.

DECLARATION OF INTERESTS

All authors are employees and shareholders of Ribon Therapeutics and a patent on this work has been granted (WO/2019/212946).

Received: March 18, 2020
Revised: May 18, 2020
Accepted: June 15, 2020
Published: July 16, 2020

REFERENCES

Abdelkarim, G.E., Gertz, K., Harms, C., Katchanov, J., Dirnagl, U., Szabo, C., and Endres, M. (2001). Protective effects of PJ34, a novel, potent inhibitor of poly(ADP-ribose) polymerase (PARP) in in vitro and in vivo models of stroke. Int. J. Mol. Med. *7*, 255–260.

Bouzo-Lorenzo, M., Stoddart, L.A., Xia, L., AP, I.J., Heitman, L.H., Briddon, S.J., and Hill, S.J. (2019). A live cell NanoBRET binding assay allows the study of ligand-binding kinetics to the adenosine A3 receptor. Purinergic Signal. *15*, 139–153.

Butepage, M., Eckei, L., Verheugd, P., and Luscher, B. (2015). Intracellular mono-ADP-ribosylation in signaling and disease. Cells *4*, 569–595.

Carlile, G.W., Robert, R., Matthes, E., Yang, Q., Solari, R., Hatley, R., Edge, C.M., Hanrahan, J.W., Andersen, R., Thomas, D.Y., et al. (2016). Latonduine analogs restore F508del-cystic fibrosis transmembrane conductance regulator trafficking through the modulation of poly-ADP ribose polymerase 3 and poly-ADP ribose polymerase 16 activity. Mol. Pharmacol. *90*, 65–79.

Carter-O'Connell, I., Jin, H., Morgan, R.K., Zaja, R., David, L.L., Ahel, I., and Cohen, M.S. (2016). Identifying family-member-specific targets of mono-ARTDs by using a chemical genetics approach. Cell Rep. *14*, 621–631.

Carter-O'Connell, I., Vermehren-Schmaedick, A., Jin, H., Morgan, R.K., David, L.L., and Cohen, M.S. (2018). Combining chemical genetics with proximity-dependent labeling reveals cellular targets of poly(ADP-ribose) polymerase 14 (PARP14). ACS Chem. Biol. *13*, 2841–2848.

Chen, J., Lam, A.T., and Zhang, Y. (2018). A macrodomain-linked immunosorbent assay (MLISA) for mono-ADP-ribosyltransferases. Anal. Biochem. *543*, 132–139.

Copeland, R.A. (2005). Evaluation of enzyme inhibitors in drug discovery. A guide for medicinal chemists and pharmacologists. Methods Biochem. Anal. *46*, 1–265.

Copeland, R.A. (2016). The drug-target residence time model: a 10-year retrospective. Nat. Rev. Drug Discov. *15*, 87–95.

Copeland, R.A., Basavapathruni, A., Moyer, M., and Scott, M.P. (2011). Impact of enzyme concentration and residence time on apparent activity recovery in jump dilution analysis. Anal. Biochem. *416*, 206–210.

Feijs, K.L., Kleine, H., Braczynski, A., Forst, A.H., Herzog, N., Verheugd, P., Linzen, U., Kremmer, E., and Luscher, B. (2013). ARTD10 substrate identification on protein microarrays: regulation of GSK3beta by mono-ADP-ribosylation. Cell Commun. Signal *11*, 5.

Haikarainen, T., Krauss, S., and Lehtio, L. (2014a). Tankyrases: structure, function and therapeutic implications in cancer. Curr. Pharm. Des. *20*, 6472–6488.

Haikarainen, T., Narwal, M., Joensuu, P., and Lehtio, L. (2014b). Evaluation and structural basis for the inhibition of tankyrases by PARP inhibitors. ACS Med. Chem. Lett. *5*, 18–22.

Ji, M., Wang, L., Xue, N., Lai, F., Zhang, S., Jin, J., and Chen, X. (2018). The development of a biotinylated NAD(+)-applied human poly(ADP-ribose) polymerase 3 (PARP3) enzymatic assay. SLAS Discov. *23*, 545–553.

Johannes, J.W., Almeida, L., Daly, K., Ferguson, A.D., Grosskurth, S.E., Guan, H., Howard, T., Ioannidis, S., Kazmirski, S., Lamb, M.L., et al. (2015). Discovery of AZ0108, an orally bioavailable phthalazinone PARP inhibitor that blocks centrosome clustering. Bioorg. Med. Chem. Lett. *25*, 5743–5747.

Jwa, M., and Chang, P. (2012). PARP16 is a tail-anchored endoplasmic reticulum protein required for the PERK- and IRE1alpha-mediated unfolded protein response. Nat. Cell. Biol. *14*, 1223–1230.

Karlberg, T., Thorsell, A.G., Kallas, A., and Schuler, H. (2012). Crystal structure of human ADP-ribose transferase ARTD15/PARP16 reveals a novel putative regulatory domain. J. Biol. Chem. *287*, 24077–24081.

Kirby, I.T., Kojic, A., Arnold, M.R., Thorsell, A.G., Karlberg, T., Vermehren-Schmaedick, A., Sreenivasan, R., Schultz, C., Schuler, H., and Cohen, M.S. (2018). A potent and selective PARP11 inhibitor suggests coupling between cellular localization and catalytic activity. Cell Chem. Biol. *25*, 1547–1553.e12.

Kunze, F.A., and Hottiger, M.O. (2019). Regulating immunity via ADP-ribosylation: therapeutic implications and beyond. Trends Immunol. *40*, 159–173.

Lebakken, C.S., Hee Chol, K., and Vogel, K.W. (2007). A fluorescence lifetime based binding assay to characterize kinase inhibitors. J. Biomol. Screen. *12*, 828–841.

Leutert, M., Pedrioli, D.M.L., and Hottiger, M.O. (2016). Identification of PARP-specific ADP-ribosylation targets reveals a regulatory function for ADP-ribosylation in transcription elongation. Mol. Cell *63*, 181–183.

Lindgren, A.E., Karlberg, T., Thorsell, A.G., Hesse, M., Spjut, S., Ekblad, T., Andersson, C.D., Pinto, A.F., Weigelt, J., Hottiger, M.O., et al. (2013). PARP inhibitor with selectivity toward ADP-ribosyltransferase ARTD3/PARP3. ACS Chem. Biol. *8*, 1698–1703.

Lu, A.Z., Abo, R., Ren, Y., Gui, B., Mo, J.R., Blackwell, D., Wigle, T., Keilhack, H., and Niepel, M. (2019). Enabling drug discovery for the PARP protein family through the detection of mono-ADP-ribosylation. Biochem. Pharmacol. *167*, 97–106.

Machleidt, T., Woodroofe, C.C., Schwinn, M.K., Mendez, J., Robers, M.B., Zimmerman, K., Otto, P., Daniels, D.L., Kirkland, T.A., and Wood, K.V. (2015). NanoBRET—a novel BRET platform for the analysis of protein-protein interactions. ACS Chem. Biol. *10*, 1797–1804.

Morgan, R.K., Kirby, I.T., Vermehren-Schmaedick, A., Rodriguez, K., and Cohen, M.S. (2019). Rational design of cell-active inhibitors of PARP10. ACS Med. Chem. Lett. *10*, 74–79.

Murai, J., Huang, S.Y., Das, B.B., Renaud, A., Zhang, Y., Doroshow, J.H., Ji, J., Takeda, S., and Pommier, Y. (2012). Trapping of PARP1 and PARP2 by clinical PARP inhibitors. Cancer Res. *72*, 5588–5599.

Ong, L.L., Vasta, J.D., Monereau, L., Locke, G., Ribeiro, H., Pattoli, M.A., Skala, S., Burke, J.R., Watterson, S.H., Tino, J.A., et al. (2020). A high-throughput BRET cellular target engagement assay links biochemical to cellular activity for Bruton's tyrosine kinase. SLAS Discov. *25*, 176–185.

Papeo, G., Avanzi, N., Bettoni, S., Leone, A., Paolucci, M., Perego, R., Quartieri, F., Riccardi-Sirtori, F., Thieffine, S., Montagnoli, A., et al. (2014). Insights into PARP inhibitors' selectivity using fluorescence polarization and

surface plasmon resonance binding assays. J. Biomol. Screen. *19*, 1212–1219.

Peng, B., Thorsell, A.G., Karlberg, T., Schuler, H., and Yao, S.Q. (2017). Small molecule microarray based discovery of PARP14 inhibitors. Angew. Chem. Int. Ed. *56*, 248–253.

Renaud, J.P., Chung, C.W., Danielson, U.H., Egner, U., Hennig, M., Hubbard, R.E., and Nar, H. (2016). Biophysics in drug discovery: impact, challenges and opportunities. Nat. Rev. Drug Discov. *15*, 679–698.

Robers, M.B., Dart, M.L., Woodroofe, C.C., Zimprich, C.A., Kirkland, T.A., Machleidt, T., Kupcho, K.R., Levin, S., Hartnett, J.R., Zimmerman, K., et al. (2015). Target engagement and drug residence time can be observed in living cells with BRET. Nat. Commun. *6*, 10091.

Schenkel, L.B., Vasbinder, M.M., Kuntz, K.W., Swinger, K.K. (2019). Quinazolinones as PARP14 inhibitors. International Patent WO/2019/126443, filed on December 20, 2018 and granted on June 27, 2019.

Thorsell, A.G., Ekblad, T., Karlberg, T., Low, M., Pinto, A.F., Tresaugues, L., Moche, M., Cohen, M.S., and Schuler, H. (2017). Structural basis for potency and promiscuity in poly(ADP-ribose) polymerase (PARP) and tankyrase inhibitors. J. Med. Chem. *60*, 1262–1271.

Vasbinder, M.M., Schenkel, L.B., Swinger, K.K., Kuntz, K.W. (2019). Pyridazinones as PARP7 Inhibitors. International Patent WO/2019/212937, filed April 29, 2019 and granted July 11, 2019.

Venkannagari, H., Fallarero, A., Feijs, K.L., Luscher, B., and Lehtio, L. (2013). Activity-based assay for human mono-ADP-ribosyltransferases ARTD7/PARP15 and ARTD10/PARP10 aimed at screening and profiling inhibitors. Eur. J. Pharm. Sci. *49*, 148–156.

Venkannagari, H., Verheugd, P., Koivunen, J., Haikarainen, T., Obaji, E., Ashok, Y., Narwal, M., Pihlajaniemi, T., Luscher, B., and Lehtio, L. (2016). Small-molecule chemical probe rescues cells from mono-ADP-ribosyltransferase ARTD10/PARP10-induced apoptosis and sensitizes cancer cells to DNA damage. Cell Chem. Biol. *23*, 1251–1260.

Vyas, S., and Chang, P. (2014). New PARP targets for cancer therapy. Nat. Rev. Cancer *14*, 502–509.

Vyas, S., Matic, I., Uchima, L., Rood, J., Zaja, R., Hay, R.T., Ahel, I., and Chang, P. (2014). Family-wide analysis of poly(ADP-ribose) polymerase activity. Nat. Commun. *5*, 4426.

Wahlberg, E., Karlberg, T., Kouznetsova, E., Markova, N., Macchiarulo, A., Thorsell, A.G., Pol, E., Frostell, A., Ekblad, T., Oncu, D., et al. (2012). Family-wide chemical profiling and structural analysis of PARP and tankyrase inhibitors. Nat. Biotechnol. *30*, 283–288.

Wang, S., Han, L., Han, J., Li, P., Ding, Q., Zhang, Q.J., Liu, Z.P., Chen, C., and Yu, Y. (2019). Uncoupling of PARP1 trapping and inhibition using selective PARP1 degradation. Nat. Chem. Biol. *12*, 1223–1231.

Wigle, T.J., Church, W.D., Majer, C.R., Swinger, K.K., Aybar, D., Schenkel, L.B., Vasbinder, M.M., Brendes, A., Beck, C., Prahm, M., et al. (2019). Forced self-modification assays as a strategy to screen MonoPARP enzymes. SLAS Discov. *3*, 241–252.

Yang, C.S., Jividen, K., Spencer, A., Dworak, N., Ni, L., Oostdyk, L.T., Chatterjee, M., Kusmider, B., Reon, B., Parlak, M., et al. (2017). Ubiquitin modification by the E3 ligase/ADP-ribosyltransferase Dtx3L/Parp9. Mol. Cell *66*, 503–516 e505.

Yoneyama-Hirozane, M., Matsumoto, S.I., Toyoda, Y., Saikatendu, K.S., Zama, Y., Yonemori, K., Oonishi, M., Ishii, T., and Kawamoto, T. (2017). Identification of PARP14 inhibitors using novel methods for detecting auto-ribosylation. Biochem. Biophys. Res. Commun. *486*, 626–631.

Yuen, L.H., Dana, S., Liu, Y., Bloom, S.I., Thorsell, A.G., Neri, D., Donato, A.J., Kireev, D., Schuler, H., and Franzini, R.M. (2019). A focused DNA-encoded chemical library for the discovery of inhibitors of NAD(+)-dependent enzymes. J. Am. Chem. Soc. *141*, 5169–5181.

Zhang, J.H., Chung, T.D., and Oldenburg, K.R. (1999). A simple statistical parameter for use in evaluation and validation of high throughput screening assays. J. Biomol. Screen. *4*, 67–73.

STAR★METHODS

KEY RESOURCES TABLE

REAGENT or RESOURCE	SOURCE	IDENTIFIER
Chemicals, Peptides, and Recombinant Proteins		
PARP1 (full-length)	Wigle et al., *SLAS Discovery* (2019)	N/A
PARP2 (full-length)	Wigle et al., *SLAS Discovery* (2019)	N/A
PARP3 (full-length)	Wigle et al., *SLAS Discovery* (2019)	N/A
PARP4 (truncate)	Wigle et al., *SLAS Discovery* (2019)	N/A
PARP5a (truncate)	Wigle et al., *SLAS Discovery* (2019)	N/A
PARP6 (truncate)	Wigle et al., *SLAS Discovery* (2019)	N/A
PARP7 (truncate)	Wigle et al., *SLAS Discovery* (2019)	N/A
PARP8 (truncate)	Wigle et al., *SLAS Discovery* (2019)	N/A
PARP9 (full-length)	Wigle et al., *SLAS Discovery* (2019)	N/A
PARP10 (truncate)	Wigle et al., *SLAS Discovery* (2019)	N/A
PARP11 (full-length)	Wigle et al., *SLAS Discovery* (2019)	N/A
PARP12 (truncate)	Wigle et al., *SLAS Discovery* (2019)	N/A
PARP13 (full-length)	Wigle et al., *SLAS Discovery* (2019)	N/A
PARP14 (truncate)	Wigle et al., *SLAS Discovery* (2019)	N/A
PARP15 (truncate)	Wigle et al., *SLAS Discovery* (2019)	N/A
PARP16 (full-length)	Wigle et al., *SLAS Discovery* (2019)	N/A
PJ-34	AdooQ Biosciences	Cat. # A15215
Olaparib	AdooQ Biosciences	Cat. # A10111
Niraparib	Selleckem	Cat. # S2741
Rucaparib	Selleckem	Cat. # S1098
Veliparib	Selleckem	Cat. # S1004
Talazoparib	Selleckem	Cat. # S7048
RBN010860	This paper	N/A
RBN011147	This paper	N/A
RBN011198	This paper	N/A
RBN011829	This paper	N/A
RBN012148	This paper	N/A
RBN012337	This paper	N/A
RBN013283	This paper	N/A
NAD^+	Millipore Sigma	Cat. # N0632
Biotin-NAD^+	Biolog	Cat. # N012
Doxycycline	Millipore Sigma	Cat. # D3072
HEPES pH = 7.5	Alfa Aesar	Cat. # J60712
NaCl	Quality Biological	Cat. # 351-036-721
Tween 20	Thermo	Cat. # 28320
DPTA-purified BSA	Perkin Elmer	Cat. # CR84-100
Dithiothreitol	Fisher Scientific	Cat. # BP172-25
TBS-T	Hoefer	Cat. # GR154-1
PBS-T	Boston Bioproducts	Cat. # IBB-645
Methanol	Fisher Scientific	Cat. # A412-1
DMSO	Millipore Sigma	Cat. # D8418
MEM + Glutamax media	Thermo	Cat. # 41090036
OptiMEM media	Thermo	Cat. # 11058021
DMEM media	Thermo	Cat. # 10569010

(*Continued on next page*)

Continued

REAGENT or RESOURCE	SOURCE	IDENTIFIER
Fetal bovine serum	VWR	Cat. # 97068-085
FuGENE(R) HD Transfection Reagent	Promega	Cat. # E2312
Critical Commercial Assays		
Europium-labeled streptavidin	Perkin Elmer	Cat. # AD0063
ULight-labeled streptavidin	Perkin Elmer	Cat. # AD0062
Europium-labeled anti-His	Perkin Elmer	Cat. # AD0111; RRID: AB_2811261
Ulight-labeled anti-His	Perkin Elmer	Cat. # TRF0105
384-well nickel-NTA coated microplates	Thermo	Custom
DELFIA Eu-N1 Streptavidin	Perkin Elmer	Cat. # 1244-360
DELFIA Assay Buffer	Perkin Elmer	Cat. # 1244-111
DELFIA Enhancement Solution	Perkin Elmer	Cat. # 1244-105
IntracellularTE Nano-Glo(R) Substrate/Inhibitor	Promega	Cat. # N2161
Deposited Data		
Structure of PARP16 bound to RBN010860	This paper	PDB: 6W65
Experimental Models: Cell Lines		
293T cells	ATCC	Cat. # CRL-3216; RRID: CVCL_0063
Oligonucleotides		
Activating dsDNA for PARP1 (5' ACCCTGCTGTGGGC/ideoxyU/GGAGAACAAGGTGAT and 3' ATCACCTTGT TCTCCAHGCCCACAGCAGGGT)	IDT DNA	Custom synthesis
Activating dsDNA for PARP2 (5'/phosphate/ GCCTATAGGC and 3'/phosphate/GCCTATACCG)	IDT DNA	Custom synthesis
Activating ssDNA for PARP3 (/phosphate/GCTGGCT TCGTAAGAAGCCAGCTCGCGGTCAGCTTGCTGACCGCG)	IDT DNA	Custom synthesis
Recombinant DNA		
pcDNA3.1 plasmid	This paper	N/A
pcDNA3.1 with human PARP1 amino acids 1 1014 with C-terminal or N-terminal NanoLuc tag	This paper	N/A
pcDNA3.1 with human PARP3 amino acids 1 – 533 with C-terminal or N-terminal NanoLuc tag	This paper	N/A
pcDNA3.1 with human PARP7 amino acids 1-657 insert with C-terminal or N-terminal NanoLuc tag	This paper	N/A
pcDNA3.1 with human PARP7 amino acids 456-657 insert with C-terminal or N-terminal NanoLuc tag	This paper	N/A
pcDNA3.1 with human PARP10 amino acids 808-1025 with C-terminal or N-terminal NanoLuc tag	This paper	N/A
pcDNA3.1 with human PARP10 amino acids 1-1025 with C-terminal or N-terminal NanoLuc tag	This paper	N/A
pcDNA3.1 with human PARP11 amino acids 1-338 with C-terminal or N-terminal NanoLuc tag	This paper	N/A
pcDNA3.1 with human PARP12 amino acids 1-701 with C-terminal or N-terminal NanoLuc tag	This paper	N/A
pcDNA3.1 with human PARP14 amino acids 1611-1801 with C-terminal or N-terminal NanoLuc tag	This paper	N/A
pcDNA3.1 with human PARP14 amino acids 1-1801 with C-terminal or N-terminal NanoLuc tag	This paper	N/A
pcDNA3.1 with human PARP16 amino acids 1-322 with C-terminal or N-terminal NanoLuc tag	This paper	N/A

(*Continued on next page*)

Continued

REAGENT or RESOURCE	SOURCE	IDENTIFIER
Other		
Envision platereader	Perkin Elmer	Cat. # 2101-0010
Biacore T200 SPR instrument	GE Healthcare	Cat. # 28975001
Streptavidin SPR chips	GE Healthcare	Cat. # 29104992
NTA SPR chips	GE Healthcare	Cat. # 28994951
Odyssey CLX infrared imager	Licor	Cat. # 9140

RESOURCE AVAILABILITY

Lead Contact

All requests for reagents and resources should be directed to the lead contact, Tim J. Wigle (twigle@ribontx.com).

Materials Availability

All unique/stable reagents generated in this study are available from the Lead Contact with a completed Materials Transfer Agreement as long as stocks remain available.

Data Code and Availability

The coordinates for the protein structure reported in this paper have been deposited in Protein Data Bank (http://www.rcsb.org/pdb) under ID code 6W65.

EXPERIMENTAL MODEL AND SUBJECT DETAILS

Cell Lines

293T cells (ATCC) expressing PARP-NanoLuc fusion proteins were grown Dulbecco's modified Eagle's medium (DMEM) supplemented with 10% heat inactivated fetal bovine serum (VWR) in a 5% CO_2 environment at 37°C.

METHOD DETAILS

Recombinant Protein Production

Recombinant PARP enzymes were expressed and purified as described previously (Wigle et al., 2019). PARP enzymes were purified to greater than 80% purity using an N-terminal hexahistidine (His6) tag. Construct, expression, and purification details can be found in Table S2. The His6 tag was left on the protein following purification in order to capture the protein on the Ni-NTA plates in the assays. Constructs with Avi tags were biotinylated by BirA either *in vitro* using recombinant enzyme or in cellulo using bacterial cell lines expressing BirA and confirmed to have close to 100% modification via mass spectrometry. Protein purity was assessed on a Bioanalyzer 2100 (Agilent; Santa Clara, CA) and only proteins with >80% purity were used in assay development.

TR-FRET Probe Displacement Assays

Displacement of RBN011147 from the NAD^+-binding site of PARP monoenzymes was measured *in vitro* using a TR-FRET assay. A Mosquito (TTP Labtech) was used to add 20 nL of a dose response curve of each test compound in DMSO into black 384-well polystyrene Proxiplates (Perkin Elmer) and a Multidrop Combi (Thermo Scientific) was used to add the rest of the reagents. Reactions were performed in an 8 μL volume by adding 6 μL of the PARP monoenzyme and RBN011147 in 1X TR-FRET assay buffer (20 mM HEPES pH = 8, 100 mM NaCl, 0.1% bovine serum albumin, 2 mM DTT and 0.002% Tween20), incubating with test compound at 25°C for 30 min, then adding 2 μL of ULight-anti 6xHis and LANCE Eu-W1024 labeled streptavidin (configuration 1) or 2 μL of ULight-streptavidin and LANCE Eu-W1024 Anti-6xHis (configuration 2). The final concentrations of PARP monoenzyme, RBN011147, ULight-anti 6xHis and LANCE Eu-W1024 labeled streptavidin or ULight-streptavidin and LANCE Eu-W1024 Anti-6xHis for each assay are listed in Table S3. Binding reactions were equilibrated at 25°C for an additional 30 min, then read on an Envision plate reader equipped with a LANCE/DELFIA top mirror using excitation = 320 nm and emission = 615 nm and 665 nM with a 90 μs delay (Perkin Elmer). The ratio of the 665/615 nm emission was calculated for each well to determine the relative amounts of PARP monoenzyme and RBN011147 complex formed in each well.

NanoBRET Probe Displacement Assays

Displacement of RBN011198 binding to NanoLuc-tagged PARP monoenzymes was measured in live cells using a bioluminescence resonance energy transfer (NanoBRET) assay. Expression plasmids were created by inserting synthesized genes for each PARP enzyme into pCDNA3.1(-) vectors coding for either N- and C-terminal NanoLuc fusions. Plasmids were prepared for transfection by diluting in DMEM + 6% FuGENE HD and adding empty vector. A volume of 2.4 mL of diluted plasmid was added to 2 x 10^7

293T cells and incubated for 24 h under standard growth conditions then used in the NanoBRET assay. Transfected cells were re-suspended in phenol red free OptiMEM to a concentration of 2.5 x 10^5 cells/mL and the NanoBRET probe was added. The plasmid information and conditions for each transfection and assay are indicated in Table S4 for H-Y-(I/L-Y) PARPs and Table S5 for H-Y-E PARPs. Next, 40 μL of cells were then added to white polystyrene 384-well non-binding surface microplate (Corning) using a Multidrop Combi (Thermo Scientific) and 40 nL of a dose response curve of each test compound in DMSO was added to the cell plate using a Mosquito (TTP Labtech). The plate was incubated in a 5% CO_2 environment at 37°C for 2 h, then 20 μL per well of a solution consisting of a 1:166 dilution of Nano-Glo substrate (Promega) and a 1:500 dilution of NanoLuc extracellular inhibitor (Promega) in phenol red free OptiMEM was added to each well. Filtered luminescence was measured on an Envision plate reader equipped with a dual 585 nm mirror, 460 ± 40 nm bandpass filter (donor) and 610 ± 50 nm longpass filter (acceptor) (Perkin Elmer). K_d^{app} values were calculated using a 4-parameter fit in Graphpad Prism Version 8.

Cellular Binding Kinetics

Measurement of cellular binding kinetics was performed using the cellular probe displacement assay as previously described (Robers et al., 2015). Briefly, 293T cells were transfected with either PARP7 or PARP14 fused to a NanoLuc tag as described above. Cells were incubated with DMSO or test compound 10-fold above the IC_{50} for 1 h at 37°C. The cells were washed with PBS and resuspended in OptiMEM, then 40 μL of cells were plated into the white non-binding surface 384-well microplate (Corning) using a Multidrop Combi (Thermo). NanoGlo substrate with extracellular inhibitor was added with RBN011198 at a concentration 10-fold above the K_d. The BRET ratio was measured on the Envision plate reader immediately and then at multiple time points for 60 min. The data were fit using a one-phase exponential association model in Graphpad Prism Version 8.

Self-Modification Enzyme Assays

Measurement of inhibition of self-modification enzyme activity was done as previously described (Wigle et al., 2019). Reactions were performed in a 25 μL volume in 384-well white polystyrene Ni-NTA coated microplates at 25°C. Enzyme assay buffer was 20 mM HEPES (pH = 7.5), 100 mM NaCl, 2 mM DTT, 0.1% DTPA-purified BSA and 0.002% Tween 20. Compounds were stored in 100% DMSO and 0.5 μL were dry-spotted into the microplates. Uninhibited control wells contained DMSO (final concentration, f.c. = 2%) and fully inhibited control wells contained rucaparib or RBN010860 (f.c. = 200 μM), depending on the PARP being tested. His-tagged PARP enzymes were added in a 20 μL volume to the microplates and incubated for 30 min before the addition of 5 μL of biotinylated-NAD^+ to initiate the reaction. The assays were ended while in the linear range of product versus time formation by the addition of 5 μL of NAD^+ (f.c. = 2 mM) to outcompete the incorporation of biotinylated-NAD^+. The details on concentrations of enzyme, biotinylated-NAD^+ and reaction time for each PARP are indicated in Table S6. Quenched reactions were washed five times using 100 μL of Tris-buffered saline + Tween 20 (TBS-T), followed by addition of 1:1000 DELFIA Eu-N1 streptavidin diluted in DELFIA assay buffer, then incubated for 30 min at 25°C to allow the streptavidin to bind to the incorporated biotin. Next, the reactions were washed five times with 100 μL TBS-T, followed by addition of 25 μL of DELFIA enhancement solution. Microplates were incubated 30 minutes, then the DELFIA signal was read on an Envision plate reader (excitation = 340 nm, emission = 615 nm).

Surface Plasmon Resonance (SPR)

The binding affinity of the compounds were assessed using protein constructs and SPR conditions as previously described (Wigle et al., 2019). PARP SPR buffer was 50 mM HEPES (pH = 7.5), 100 mM NaCl, 1 mM TCEP, 0.05% Tween 20 and assays were run at 25°C. PARPs were either captured via N-terminal His6 tags on CM5 Ni-NTA sensor chips or via N-terminal biotinylated Avi tags on streptavidin SA sensor chips (GE Healthcare Life Sciences; Marlborough, MA). The constructs used in the SPR assay are listed in Table S2. Typically, 3000 – 6000 RU of protein were immobilized for each assay. Compounds were screened using a flow rate of 30 μL/min, using 60 s of association time, typically followed by observing dissociation for 90 s. For higher affinity compounds the dissociation window was increased and in some instances compound binding was analyzed using single-cycle kinetics. Solvent correction was applied using a 6-point curve from 1.5 – 2.75 % DMSO injected before and after every 96 cycles. Data were fit using Biacore software to an equilibrium binding model to derive the binding constant K_D, and when significant off-rates (> 120 s) were observed, data were fit to a kinetic model to derive parameters for association and dissociation (k_a and k_d) and the binding constant K_d.

X-Ray Crystallography

Tag-cleaved, purified PARP16 (20 mg/mL, 20 mM HEPES, 200 mM NaCl, 2 mM TCEP, pH = 7.5) was incubated with a weak binding fragment at 2 mM and crystallized via the sitting drop method of vapor diffusion using a drop size of 0.5 μL protein and 0.5 μL well solution (100 mM sodium citrate pH = 5.5, 18% w/v PEG3350). A crystal was then transferred to a soaking solution containing 2 mM RBN010860, 100 mM sodium citrate pH = 5.5, 18% w/v PEG3350 for 6 h. The crystal was cryoprotected in a solution containing 85% soaking solution and 15% glycerol prior to vitrification in liquid nitrogen. Data reduction and scaling were performed using XDS. Structure determination was performed by molecular replacement using the published PARP16 structure, PDBID 4F0D (Karlberg et al., 2012), as a search model and REFMAC5 program in CCP4 software. After manual ligand placement, iterative cycles of refinement and model building were performed using REFMAC5 and COOT, respectively. The crystal structure was deposited into the Protein Data Bank with PDB code 6W65. Data collection and refinement statistics are shown in Table S8. After manual ligand placement, iterative cycles of refinement and model building were performed using REFMAC5 and COOT, respectively.

General Chemical Synthesis

All reactions were run in standard glassware under air or nitrogen, as noted. The purity of all final compounds was >95% as determined by HPLC using the instrumentation and methods described below. Solvents were purchased commercially and used without additional drying or purification. 2,5-dioxopyrrolidin-1-yl 3-(5,5-difluoro-7-(1*H*-pyrrol-2-yl)-5*H*-5λ^4,6λ^4-dipyrrolo[1,2-*c*:2',1'-*f*][1,3,2]diazaborinin-3-yl)propanoate (NanoBRET 590SE) was purchased from Promega. Abbreviations: ACN (acetonitrile); DCM (dichloromethane); DIPEA (diisopropylethylamine); DMF (dimethylformamide); EtOAc (ethyl acetate); h (hours); HATU (1-[bis(dimethylamino)methylene]-1H-1,2,3-triazolo[4,5-b]pyridinium 3-oxide hexafluorophosphate); HCl (hydrochloric acid); MeOH (methanol); NMP (N-methyl-2-pyrrolidone); rt (room temperature); SEMCl (2-(trimethylsilyl)ethoxymethyl chloride); TEA (triethyl amine); TFA (trifluoroacetic acid).

^{1}H NMR spectra were recorded at 400 MHz using a Bruker AVANCE 400 MHz spectrometer. NMR interpretation was performed using MestReC, MestReNova or Bruker Topspin software to assign chemical shift and multiplicity. In cases where two adjacent peaks of equal or unequal height were observed, these two peaks may be labeled as either a multiplet or as a doublet. In the case of a doublet, a coupling constant using this software may be assigned. In any given example, one or more protons may not be observed due to obscurity by water and/or solvent peaks. LC-MS equipment and conditions are as follows:

LC: Agilent Technologies 1290 series, Binary Pump, Diode Array Detector. Agilent Poroshell 120 EC- C18, 2.7 μm, 4.6×50 mm column. Mobile phase: A: 0.05% formic acid in water (v/v), B: 0.05% formic acid in ACN (v/v). Flow Rate: 1 mL/min at 25°C. Detector: 214 nm, 254 nm. Gradient stop time, 10 min. Timetable:

T (min)	A (%)	B (%)
0.0	90	10
0.5	90	10
8.0	10	90
10.0	0	100

MS: G6120A, Quadrupole LC/MS, Ion Source: ES-API, TIC: 70∼1000 m/z, Fragmentor: 60, Drying gas flow: 10 L/min, Nebulizer pressure: 35 psi, Drying gas temperature: 350°C, Vcap: 3000V.

LC Shimadzu LC-20AD, Binary Pump, Diode Array Detector. Column: Ascentis Express C18, 50*3.0 mm, 2.7 μm. Mobile phase: A: Water/0.05%TFA, B: Acetonitrile/0.05%TFA. Flow Rate: 1.5 mL/min at 40°C. Detector: 254 nm, 220 nm. Gradient stop time, 2.9 min. Timetable:

T (min)	A (%)	B (%)
0.01	90	5
2.10	5	95
2.70	5	95
2.90	90	5

MS: LC-MS-2020, Quadrupole LC/MS, Ion Source: ES-API, TIC: 90∼900 m/z, Fragmentor: 60, Drying gas flow: 15 L/min, Nebulizing Gas Flow: 1.5 L/min, Drying gas temperature: 250°C, Vcap: 1100V.

Sample preparation: samples were dissolved in ACN or MeOH at 1∼10 mg/mL, then filtered through a 0.22 μm filter membrane. Injection volume: 1∼10 μL.

Synthesis of 5-[5-(Piperidin-4-yloxy)-2,3-dihydro-1*H*-isoindol-2-yl]-4-(trifluoromethyl)-2,3-dihydropyridazin-3-one (RBN010860)

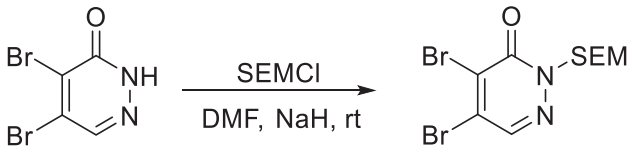

4,5-Dibromo-2-[[2-(trimethylsilyl)ethoxy]methyl]-2,3-dihydropyridazin-3-one

To a solution of 4,5-dibromo-2,3-dihydropyridazin-3-one (3500 g, 13.78 mol, 1.00 equiv) in DMF (30 L) was added sodium hydride (400 g, 16.56 mol, 1.20 equiv) in batches at 0°C under nitrogen. The resulting solution was stirred for 1 hour at room temperature, then [2-(chloromethoxy)ethyl]trimethylsilane (2500 g, 15.2 mol, 1.10 equiv) was added dropwise at 0°C and stirred for 2 h at room temper-

ature. The reaction was then quenched by the addition of 30 L of water. The resulting solution was extracted with 3 x 50 L of ethyl acetate and the organic layers combined. The organic layers were washed with 3 x 30 L of brine, dried over anhydrous sodium sulfate and concentrated under reduced pressure to afford 4.2 kg of title compound. LC-MS: $[M+H]^+$ 384.70.

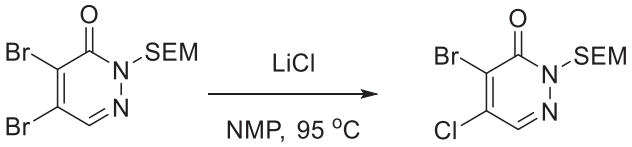

4-Bromo-5-chloro-2-[[2-(trimethylsilyl)ethoxy]methyl]-2,3-dihydropyridazin-3-one

To a solution of 4,5-dibromo-2-[[2-(trimethylsilyl)ethoxy]methyl]-2,3-dihydropyridazin-3-one (2200 g, 5.73 mol, 1.00 equiv) in NMP (6 L) was added chlorolithium (231 g, 5.73 mol, 1.00 equiv) and stirred for 4 hours at 95°C. The reaction was then diluted by the addition of 10 L of water, extracted with 3 x 20 L of ethyl acetate and the organic layers combined. The organic layers were washed with 3 x 20 L of brine, dried over anhydrous sodium sulfate and concentrated under reduced pressure. The residue was purified by column chromatography (EtOAc:petroleum ether, 1:50, v/v) to afford 4.2 kg of 4,5-dibromo-2-[[2-(trimethylsilyl)ethoxy]methyl]-2,3-dihydropyridazin-3-one. This was repeated 2 times resulting in 2.2 kg of 4-bromo-5-chloro-2-[[2-(trimethylsilyl)ethoxy]methyl]-2,3-dihydropyridazin-3-one. LC-MS: $[M+H]^+$ 340.90.

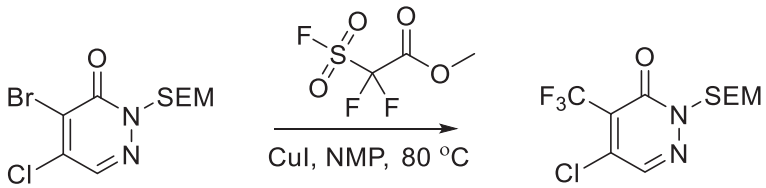

5-Chloro-4-(trifluoromethyl)-2-[[2-(trimethylsilyl)ethoxy]methyl]-2,3-dihydropyridazin-3-one

To a solution of 4-bromo-5-chloro-2-[[2-(trimethylsilyl)ethoxy]methyl]-2,3-dihydropyridazin-3-one (1100 g, 3.23 mol, 1.00 equiv) in NMP (6 L) at room temperature was added CuI (56 g, 0.64 mol, 0.20 equiv) followed by dropwise addition of methyl 2,2-difluoro-2-(fluorosulfonyl)acetate (1865 g, 9.7 mol, 3.00 equiv). The resulting solution was stirred for 2 hours at 80°C. The reaction was then quenched by the addition of 10 L of water and extracted with 3 x 10 L of ethyl acetate. The organic layers were combined and washed with 3 x 10 L of brine, dried over anhydrous sodium sulfate, and concentrated under reduced pressure. The residue was purified by column chromatography (ethyl acetate/petroleum ether, 1/100, v/v) to afford 1030 g (76%) of the title compound. LC-MS: $[M+H]^+$ 329.00; ^{1}H NMR (300 MHz, $CDCl_3$) δ 7.82 (s, 1H), 5.50 (d, *J* = 27.3 Hz, 2H), 3.74 (dt, *J* = 12.9, 8.2 Hz, 2H), 0.97 (td, *J* = 8.3, 5.0 Hz, 2H), 0.01 (d, *J* = 2.1 Hz, 9H).

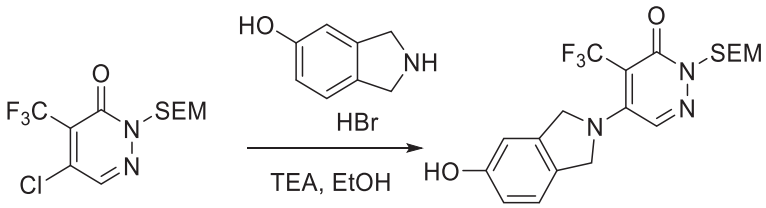

5-(5-Hydroxy-2,3-dihydro-1H-isoindol-2-yl)-4-(trifluoromethyl)-2-[[2-(trimethylsilyl)ethoxy]methyl]-2,3-dihydropyridazin-3-one

A solution of 5-chloro-4-(trifluoromethyl)-2-[[2-(trimethylsilyl)ethoxy]methyl]-2,3-dihydropyridazin-3-one (2.8 g, 8.52 mmol, 1.00 equiv), 2,3-dihydro-1H-isoindol-5-ol hydrobromide (4.27 g, 19.76 mmol, 1.00 equiv), and TEA (10 mL) in ethanol (40 mL) was stirred for 1 h at 60°C. The resulting solution was extracted with 2 x 100 mL of EtOAc and the organic layers combined and concentrated under reduced pressure to afford 4.5 g of the title compound as a yellow oil. LC-MS: $[M+H]^+$ 428.23.

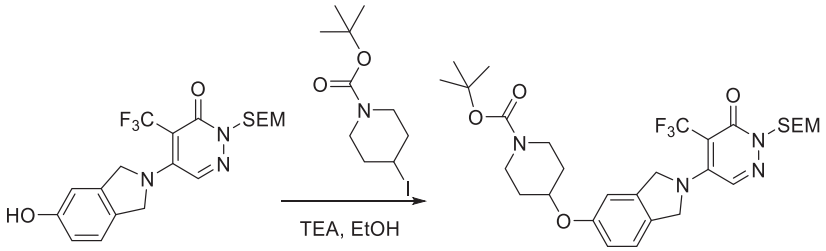

tert-Butyl 4-([2-[6-oxo-5-(trifluoromethyl)-1-[[2-(trimethylsilyl)ethoxy]methyl]-1,6-dihydropyridazin-4-yl]-2,3-dihydro-1*H*-isoindol-5-yl]oxy)piperidine-1-carboxylate

A solution of 5-(5-hydroxy-2,3-dihydro-1H-isoindol-2-yl)-4-(trifluoromethyl)-2-[[2-(trimethylsilyl)ethoxy]methyl]-2,3-dihydropyridazin-3-one (4.5 g, 10.53 mmol, 1.00 equiv), *tert*-butyl 4-iodopiperidine-1-carboxylate (20 g, 64.28 mmol, 8.00 equiv), potassium carbonate (15 g, 108.53 mmol, 10.00 equiv), and DMF (50 mL) was stirred for 2 days at 80°C. The resulting solution was extracted with 2 x 200 mL of EtOAc and the organic layers combined and concentrated under reduced pressure. The residue was applied onto a silica gel column eluting with EtOAc/petroleum ether to afford the title compound (2 g, 31%) as a yellow oil. LC-MS: $[M+H]^+$ 611.15.

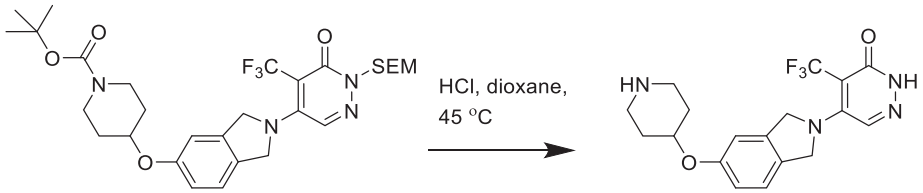

5-[5-(Piperidin-4-yloxy)-2,3-dihydro-1*H*-isoindol-2-yl]-4-(trifluoromethyl)-2,3-dihydropyridazin-3-one

A solution of *tert*-butyl 4-([2-[6-oxo-5-(trifluoromethyl)-1-[[2-(trimethylsilyl)ethoxy]methyl]-1,6-dihydropyridazin-4-yl]-2,3-dihydro-1H-isoindol-5-yl]oxy)piperidine-1-carboxylate (150 mg, 0.25 mmol, 1.00 equiv) in HCl/dioxane (5 mL) was stirred overnight at 45°C. The resulting mixture was concentrated under reduced pressure and the crude product was purified by C18 reverse phase chromatography eluting with H_2O/ACN to afford the title compound as a white solid LC-MS: $[M+H]^+$ 381.28. ^1H NMR (400 MHz, Methanol-d_4) δ 8.05 (s, 1H), 7.27 (d, J = 8.4 Hz, 1H), 7.02 – 6.91 (m, 2H), 5.00 (d, J = 10.6 Hz, 4H), 4.61 - 4.48 (m, 1H), 3.21 - 3.10 (m, 2H), 2.89 - 2.78 (m, 2H), 2.11 - 2.08 (m, 2H), 1.82 - 1.69 (m, 2H).

Synthesis of 5-[(3aS,4S,6aR)-2-Oxo-hexahydro-1*H*-thieno[3,4-d]imidazolidin-4-yl]-*N*-(6-[2-[4-([2-[6-oxo-5-(trifluoromethyl)-1,6-dihydropyridazin-4-yl]-2,3-dihydro-1*H*-isoindol-5-yl]oxy)piperidin-1-yl]acetamido]hexyl) pentanamide (RBN011147)

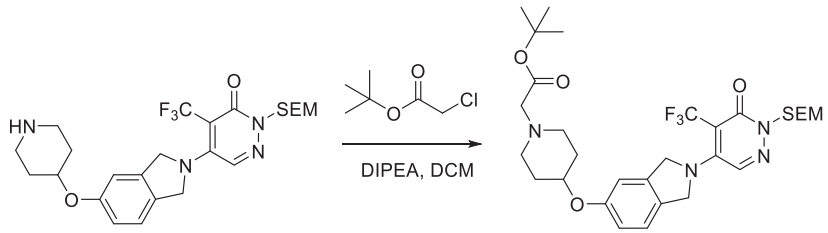

tert-Butyl 2-[4-([2-[6-oxo-5-(trifluoromethyl)-1-[[2-(trimethylsilyl)ethoxy]methyl]-1,6-dihydropyridazin-4-yl]-2,3-dihydro-1*H*-isoindol-5-yl]oxy)piperidin-1-yl]acetate

A solution of 5-[5-(piperidin-4-yloxy)-2,3-dihydro-1H-isoindol-2-yl]-4-(trifluoromethyl)-2-[[2-(trimethylsilyl)ethoxy]methyl]-2,3-dihydropyridazin-3-one (1 g, 1.96 mmol, 1.00 equiv), *tert*-butyl 2-chloroacetate (450 mg, 2.99 mmol, 3.00 equiv), DIPEA (5 mL), and dichloromethane (10 mL) was stirred overnight at 25°C. The residue was purified by C18 reverse phase chromatography eluting with H_2O/CH_3CN to afford the title compound (540 mg, 44%) as a yellow oil. LC-MS: $[M+H]^+$ 625.20.

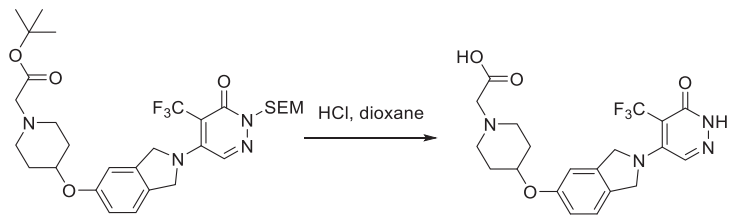

2-[4-([2-[6-Oxo-5-(trifluoromethyl)-1,6-dihydropyridazin-4-yl]-2,3-dihydro-1*H*-isoindol-5-yl]oxy)piperidin-1-yl] hydrochloride

A solution of *tert*-butyl 2-[4-([2-[6-oxo-5-(trifluoromethyl)-1-[[2-(trimethylsilyl)ethoxy]methyl]-1,6-dihydropyridazin-4-yl]-2,3-dihydro-1H-isoindol-5-yl]oxy)piperidin-1-yl]acetate (540 mg, 0.86 mmol, 1.00 equiv) and dioxane/HCl (8 mL) was stirred overnight at 25°C. The resulting mixture was concentrated under reduced pressure. The residue was purified by C18 reverse phase chromatography

eluting with H_2O/CH_3CN to afford 200 mg (53%) of title compound as a white solid. LC-MS: $[M+H]^+$ 439.31.

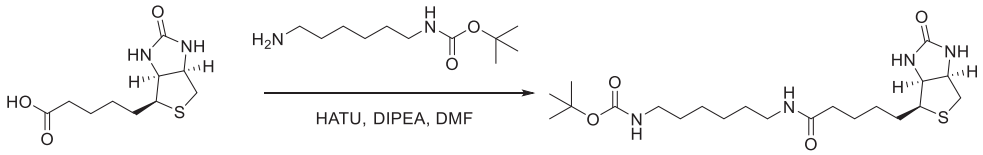

Tert-butyl *N*-(6-[5-[(3aS,4S,6aR)-2-oxo-hexahydro-1H-thieno[3,4-d]imidazolidin-4-yl]pentanamido]hexyl)carbamate

A solution of 5-[(3a*S*,4*S*,6a*R*)-2-oxo-hexahydro-1*H*-thieno[3,4-d]imidazolidin-4-yl]pentanoic acid (976 mg, 3.99 mmol, 1.00 equiv), DIPEA (1.55 g, 11.99 mmol, 3.00 equiv), HATU (1.82 g, 4.79 mmol, 1.20 equiv), *tert*-butyl N-(6-aminohexyl)carbamate (864 mg, 3.99 mmol, 1.00 equiv) in DMF (15 mL) was stirred overnight at 25°C. The reaction was then quenched by the addition of 50 mL of water. The solids were collected by filtration to afford 1.5 g (85%) of the title compound as a white solid. LC-MS: $[M+H]^+$ 443.26.

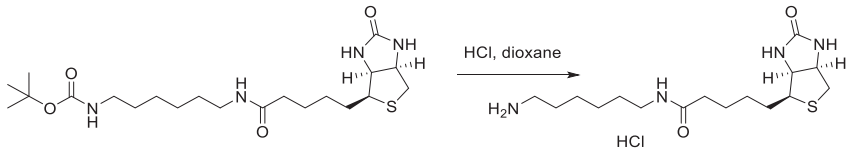

5-[(3aS,4S,6aR)-2-Oxo-hexahydro-1*H*-thieno[3,4-d]imidazolidin-4-yl]-N-(6-aminohexyl)pentanamide hydrochloride

A solution of *tert*-butyl *N*-(6-[5-[(3a*S*,4*S*,6a*R*)-2-oxo-hexahydro-1*H*-thieno[3,4-d]imidazolidin-4-yl]pentanamido]hexyl)carbamate (800 mg, 1.81 mmol, 1.00 equiv) in hydrogen chloride/dioxane (20 mL) was stirred overnight at 25°C. The resulting mixture was concentrated under reduced pressure to afford 600 mg (88%) of the title compound as a gray crude oil. LC-MS: $[M+H]^+$ 343.21.

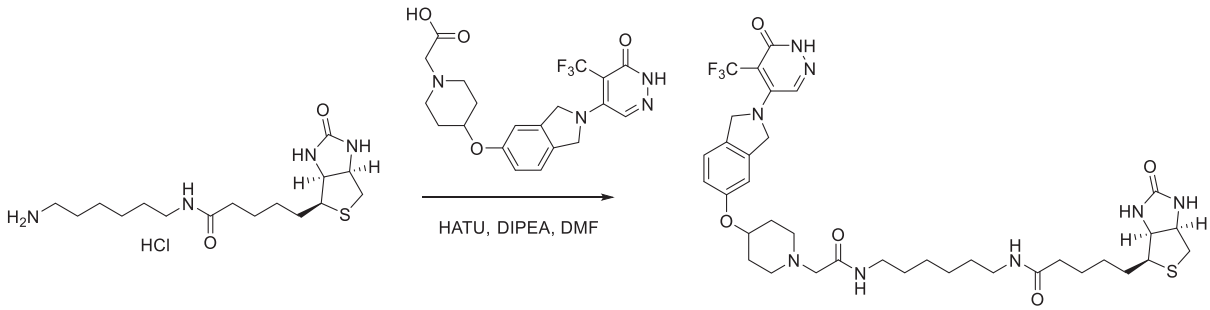

5-[(3aS,4S,6aR)-2-Oxo-hexahydro-1H-thieno[3,4-d]imidazolidin-4-yl]-*N*-(6-[2-[4-([2-[6-oxo-5-(trifluoromethyl)-1,6-dihydropyridazin-4-yl]-2,3-dihydro-1H-isoindol-5-yl]oxy)piperidin-1-yl]acetamido]hexyl)pentanamide

A solution of 2-[4-([2-[6-oxo-5-(trifluoromethyl)-1,6-dihydropyridazin-4-yl]-2,3-dihydro-1*H*-isoindol-5-yl]oxy)piperidin-1-yl]hydrochloride (175 mg, 0.40 mmol, 1.00 equiv), DIPEA (258 mg, 2.00 mmol, 5.00 equiv), HATU (228 mg, 0.60 mmol, 1.50 equiv), 5-[(3aS,4S,6aR)-2-oxo-hexahydro-1H-thieno[3,4-d]imidazolidin-4-yl]-N-(6-aminohexyl)pentanamide hydrochloride (228 mg, 0.60 mmol, 1.50 equiv) in DMF (3 mL) was stirred for 4 h at 25 ^{0}C. The crude product was purified by C18 reverse phase chromatography eluting with H_2O/CH_3CN to afford the title compound as a white solid (118.3 mg, 39%). LC-MS: $[M+H]^+$ 763.35. ^{1}H NMR (DMSO-d_6, 400 MHz) δ: 12.52 (s, 1H), 7.98 (s, 1H), 7.81 – 7.68 (m, 2H), 7.26 (d, J = 8.4 Hz, 1H), 7.00 (d, J = 2.2 Hz, 1H), 6.91 (dd, J = 8.4, 2.3 Hz, 1H), 6.45 – 6.39 (m, 1H), 6.36 (s, 1H), 4.91 (d, J = 6.1 Hz, 4H), 4.45 (m, 1H), 4.26 (m, 1H), 4.17 – 4.08 (m, 1H), 3.14 – 2.96 (m, 5H), 2.91 (s, 2H), 2.82 (dd, J = 12.4, 5.1 Hz, 1H), 2.73 – 2.63 (m, 2H), 2.58 (d, J = 12.4 Hz, 1H), 2.33 (ddd, J = 11.8, 9.4, 3.1 Hz, 2H), 2.11 – 1.90 (m, 4H), 1.76 – 1.54 (m, 3H), 1.57 – 1.20 (m, 13H).

Synthesis of 3-(5,5-difluoro-7-(1H-pyrrol-2-yl)-5H-5l4,6l4-dipyrrolo[1,2-c:2',1'-f][1,3,2]diazaborinin-3-yl)-N-(6-(2-(4-((2-(6-oxo-5-(trifluoromethyl)-1,6-dihydropyridazin-4-yl)isoindolin-5-yl)oxy)piperidin-1-yl)acetamido)hexyl) propanamide (RBN011198)

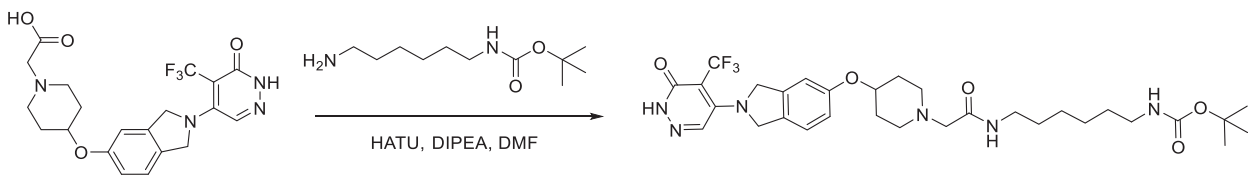

tert-Butyl *N*-(6-[2-[4-([2-[6-oxo-5-(trifluoromethyl)-1,6-dihydropyridazin-4-yl]-2,3-dihydro-1*H*-isoindol-5-yl]oxy) piperidin-1-yl]acetamido]hexyl)carbamate

A solution of 2-[4-([2-[6-oxo-5-(trifluoromethyl)-1,6-dihydropyridazin-4-yl]-2,3-dihydro-1H-isoindol-5-yl]oxy)piperidin-1-yl]acetic acid (44 mg, 0.10 mmol, 1.00 equiv), DIPEA (52 mg, 0.40 mmol, 4.00 equiv), HATU (46 mg, 0.12 mmol, 1.20 equiv), and *tert*-butyl N-(6-aminohexyl)carbamate (24 mg, 0.11 mmol, 1.10 equiv) in DMF (1 mL) was stirred overnight at 25°C. The crude product was purified by C18 reverse phase chromatography eluting with H_2O/CH_3CN to afford 38 mg (59%) of title compound as an off-white solid. LC-MS: $[M+H]^+$ 637.31.

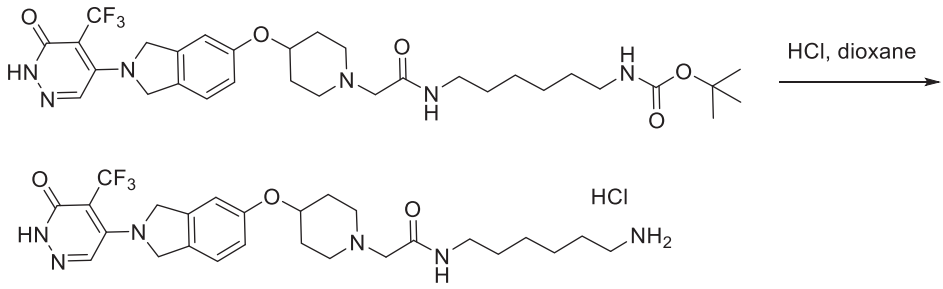

N-(6-Aminohexyl)-2-[4-([2-[6-oxo-5-(trifluoromethyl)-1,6-dihydropyridazin-4-yl]-2,3-dihydro-1*H*-isoindol-5-yl]oxy) piperidin-1-yl]acetamide hydrochloride

A solution of *tert*-butyl *N*-(6-[2-[4-([2-[6-oxo-5-(trifluoromethyl)-1,6-dihydropyridazin-4-yl]-2,3-dihydro-1H-isoindol-5-yl]oxy)piperidin-1-yl]acetamido]hexyl)carbamate (38 mg, 0.06 mmol, 1.00 equiv) in hydrogen chloride/dioxane (10 mL) was stirred for 3 hours at 25°C. The resulting mixture was concentrated under reduced pressure to afford the title compound as a gray solid (30 mg, 88%). LC-MS: $[M-Cl]^+$ 537.27.

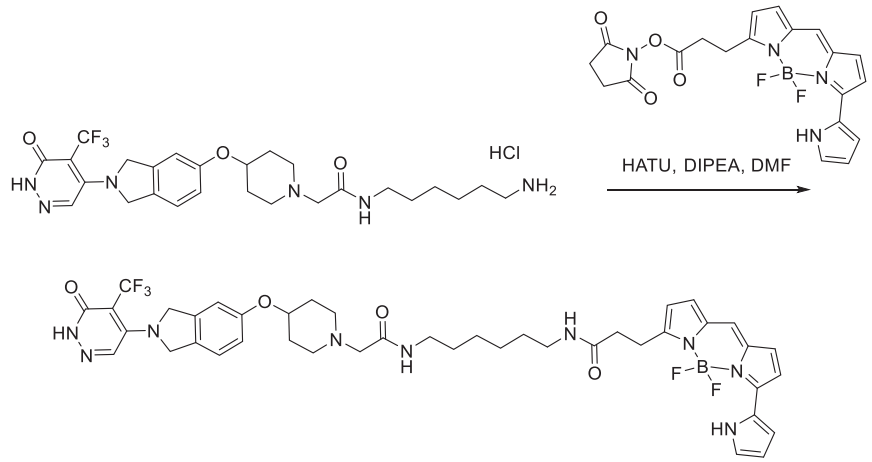

3-(5,5-difluoro-7-(1*H*-pyrrol-2-yl)-5*H*-5λ⁴,6λ⁴-dipyrrolo[1,2-c:2',1'-f][1,3,2]diazaborinin-3-yl)-*N*-(6-(2-(4-((2-(6-oxo-5-(trifluoromethyl)-1,6-dihydropyridazin-4-yl)isoindolin-5-yl)oxy)piperidin-1-yl)acetamido)hexyl)propanamide

A solution of NanoBRET 590SE (23 mg, 0.04 mmol, 2.00 equiv), DIPEA (52 mg, 0.40 mmol, 5.00 equiv), and *N*-(6-aminohexyl)-2-[4-([2-[6-oxo-5-(trifluoromethyl)-1,6-dihydropyridazin-4-yl]-2,3-dihydro-1*H*-isoindol-5-yl]oxy)piperidin-1-yl]acetamide hydrochloride (10 mg, 0.02 mmol, 1.00 equiv) in DCM (2 mL) and MeOH (2 mL) was stirred for 2 h at 25°C. The resulting mixture was concentrated under reduced pressure and the crude product was purified by C18 reverse phase chromatography eluting with H_2O/CH_3CN to afford 6.9 mg of a purple solid (35%). LC-MS: $[M+H]^+$ 848.38; ^1H NMR (CD_3OD, 400 MHz) δ: 7.98 (s,1H), 7.28 – 7.14 (m, 5H), 7.02 – 6.84 (m, 4H), 6.37 – 6.26 (m, 2H), 4.93 (d, J = 12.0 Hz, 4H), 4.45 - 4.35 (m, 1H), 3.29 – 3.13 (m, 6H), 3.01 (s, 2H), 2.81 – 2.70 (m, 2H), 2.60 (t, J = 7.7 Hz, 2H), 2.43 (td, J = 8.7, 4.6 Hz, 2H), 2.01 (dd, J = 11.8, 7.0 Hz, 2H), 1.81 (ddt, J = 15.8, 11.5, 5.5 Hz, 2H), 1.51 (q, J = 7.3, 6.8 Hz, 4H), 1.38 – 1.26 (m, 4H).

Synthesis of 3-(dimethylamino)-N-(6-oxo-5,6-dihydrophenanthridin-2-yl)propenamide (RBN011829)

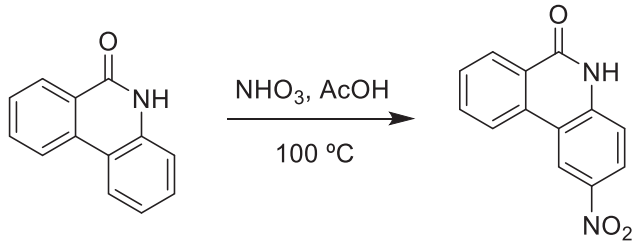

2-Nitro-5H-phenanthridin-6-one

To a solution of 5H-phenanthridin-6-one (15 g, 77 mmol, 1 equiv) in acetic acid (300 mL) was added HNO_3 (30 mL, 77 mmol, 1 equiv). The reaction was stirred at 100°C for 3 h. The mixture was cooled to room temperature and filtered, and the solid was washed with acetic acid (150 mL). Drying the solid gave the title compound (14.8 g, 61.6 mmol, 80% yield) as a white solid.

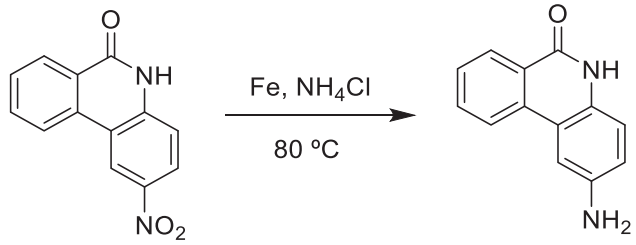

2-Amino-5H-phenanthridin-6-one

To a solution of 2-nitro-5H-phenanthridin-6-one (8.96 g, 37.3 mmol, 1 equiv) in water (50 mL) and ethanol (50 mL) was added iron (12.5 g, 224 mmol, 6 equiv) and NH_4Cl (11.98 g, 224 mmol, 6 equiv). The reaction was stirred at 80°C for 4 h and filtered while hot. The filter cake was wash with methanol (200 mL) and dried to give the title compound (4 g, 19 mmol, 51% yield) as a white solid. LC-MS: $[M+H]^+$ 211.1.

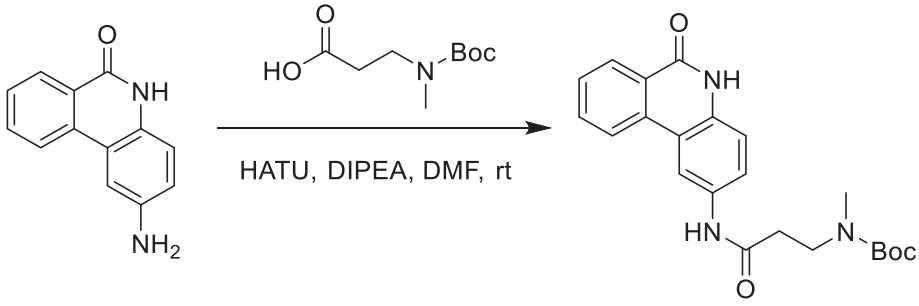

tert-Butyl N-methyl-N-[3-oxo-3-[(6-oxo-5H-phenanthridin-2-yl)amino]propyl]carbamate

To solution of 3-[*tert*-butoxycarbonyl(methyl)amino]propanoic acid (290 mg, 1.43 mmol, 1 equiv), HATU (814 mg, 2.14 mmol, 1.5 equiv) and diisopropylethyl amine (461 mg, 3.57 mmol, 2.5 equiv) in DMF (10 mL) was added 2-amino-5H-phenanthridin-6-one (300 mg, 1.43 mmol, 1 equiv), and the mixture was stirred at rt for 2 h. The mixture was quenched with water (30 mL), and extracted with DCM (30 mL x 2). The combined organic layers were washed with water (30 mL) and brine (30 mL), dried over sodium sulfate, and concentrated. The residue was purified by silica gel column chromatography (DCM/MeOH=50:1, v/v) to afford the title compound

(410 mg, 1 mmol, 73% yield) as an off-white solid. LC-MS: $[M+H\text{-}Boc]^+$ 296.1.

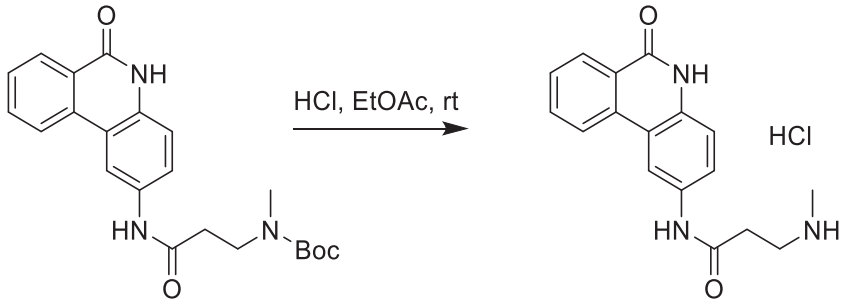

3-(Methylamino)-N-(6-oxo-5H-phenanthridin-2-yl)propanamide hydrochloride

A mixture of *tert*-butyl *N*-methyl-*N*-[3-oxo-3-[(6-oxo-5H-phenanthridin-2-yl)amino]propyl]carbamate (400 mg, 1.01 mmol, 1.0 equiv) in HCl in EtOAc (1.01 mL, 1.01 mmol, 1 equiv) was stirred at 25°C overnight. The mixture was filtered, and the cake was washed with EtOAc (10 mL). The residue was dried to afford the title compound (300 mg,0.90 mmol, 89% yield) as a gray solid. LC-MS: $[M+H]^+$ 296.1.

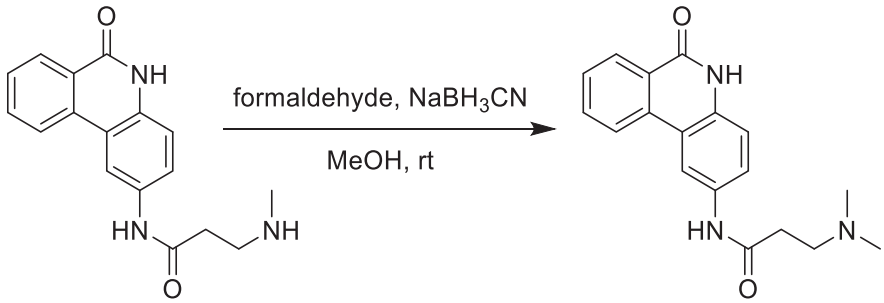

3-(dimethylamino)-N-(6-oxo-5H-phenanthridin-2-yl)propanamide

To a solution of 3-(methylamino)-N-(6-oxo-5H-phenanthridin-2-yl)propanamide hydrochloride (70 mg, 0.21 mmol, 1 equiv) in methanol (10 mL) was added formaldehyde (0.5 mL, 0.21 mmol, 1 equiv) and the reaction was stirred at room temperature for 40 min. Sodium cyanoborohydride (106 mg, 1.69 mmol, 8 equiv) was added, and the reaction was stirred at room temperature for another 2 h. The mixture was purified by preparative-TLC (DCM:MeOH = 15:1) to give the title compound (30 mg, 0.1 mmol, 46% yield) as a white solid. ^{1}H NMR (400 MHz, $DMSOd_6$) δ 11.63 (s, 1H), 10.23 (s, 1H), 8.63 (s, 1H), 8.31 (d, *J* = 7.6 Hz, 1H), 8.22 (d, *J* = 8.0 Hz, 1H), 7.87 (t, *J* = 7.6 Hz, 1H), 7.67 – 7.57 (m, 2H), 7.29 (d, *J* = 8.8 Hz, 1H), 2.75 (t, *J* = 6.8 Hz, 2H), 2.55 (t, *J* = 6.8 Hz, 2H), 2.31 (s, 6H); LC-MS: $[M+H]^+$ 310.1.

Synthesis of 3-(5,5-difluoro-7-(1H-pyrrol-2-yl)-5H-5λ^4,6λ^4-dipyrrolo[1,2-c:2',1'-f][1,3,2]diazaborinin-3-yl)-N-(6-(methyl(3-oxo-3-((6-oxo-5,6-dihydrophenanthridin-2-yl)amino)propyl)amino)hexyl)propenamide (RBN012148)

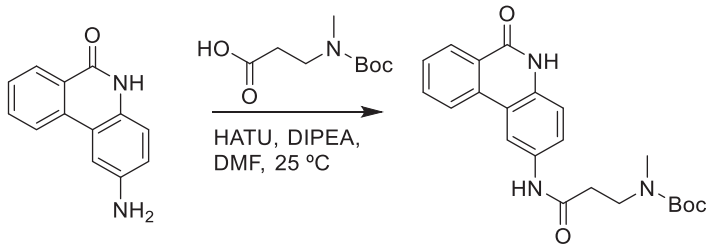

tert-Butyl N-methyl-N-[3-oxo-3-[(6-oxo-5H-phenanthridin-2-yl)amino]propyl]carbamate

To solution of 3-[*tert*-butoxycarbonyl(methyl)amino]propanoic acid (290 mg, 1.43 mmol, 1 equiv), HATU (814 mg, 2.14 mmol, 1.5 equiv) and DIPEA (461 mg, 3.57 mmol, 2.5 equiv) in DMF (10 mL) was added 2-amino-5H-phenanthridin-6-one (300 mg, 1.43 mmol, 1 equiv), and the mixture was stirred at 25°C for 2 h. The mixture was quenched with water (30 mL) and extracted twice with DCM (30 mL). The combined organic layers were washed with water (30 mL) and brine (30 mL), dried with sodium sulfate, and concentrated. The residue was purified by silica gel chromatography (DCM/MeOH=50:1, v/v) to afford the title compound (410 mg,

1.0 mmol, 73% yield) as an off-white solid. LC-MS: $[M+H]^+$ 396.2.

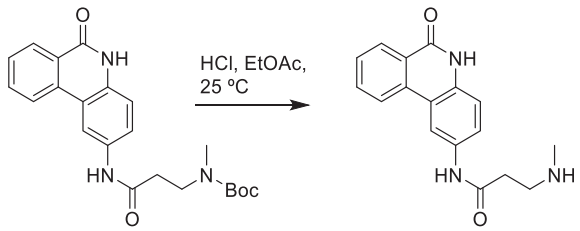

3-(Methylamino)-N-(6-oxo-5H-phenanthridin-2-yl)propanamide hydrochloride

A mixture of *tert*-butyl *N*-methyl-*N*-[3-oxo-3-[(6-oxo-5*H*-phenanthridin-2-yl)amino]propyl]carbamate (400 mg, 1.01 mmol, 1.0 equiv) in HCl in EtOAc (1.01 mL, 1.01 mmol, 1 equiv) was stirred at 25°C overnight. The mixture was filtered, and the cake was washed with EtOAc (10 mL). The residue was concentrated to afford the title compound (300 mg, 0.90 mmol, 89% yield) as a gray solid. LC-MS: $[M+H]^+$ 296.1.

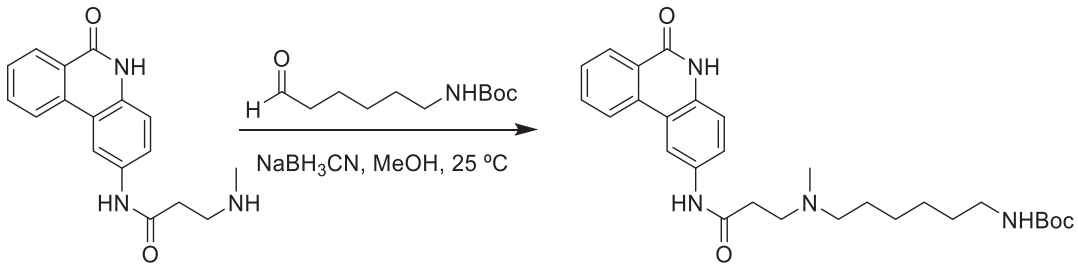

tert-Butyl N-[6-[methyl-[3-oxo-3-[(6-oxo-5H-phenanthridin-2-yl)amino]propyl]amino]hexyl]carbamate

To a stirred solution of 3-(methylamino)-*N*-(6-oxo-5H-phenanthridin-2-yl)propanamide hydrochloride (110 mg, 0.33 mmol, 1 equiv) and *tert*-butyl *N*-(6-oxohexyl)carbamate (86 mg, 0.4 mmol, 1.2 equiv) in MeOH (3 mL) at 25°C , $NaBH_3CN$ (208 mg, 3.32 mmol, 10 equiv) was added batchwise. The reaction was stirred overnight. The resulting mixture was quenched with water and extracted with EtOAc. The organic phase was washed with brine and dried over anhydrous sodium sulfate. After concentration, the crude product was purified by preparative-TLC (EtOAc/petroleum.ether = 1/2) to afford the title compound (140 mg, 0.28 mmol, 85% yield) as a white solid. LC-MS: $[M+H]^+$ 495.3.

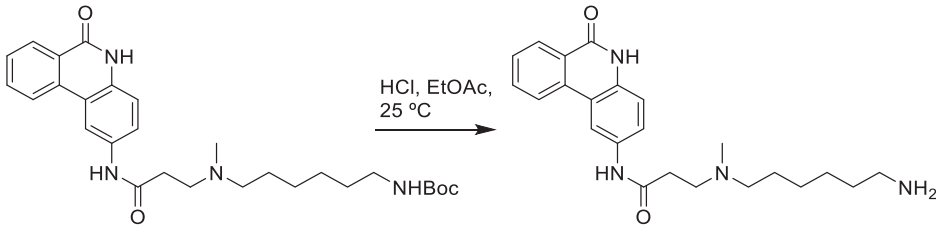

3-[6-aminohexyl(methyl)amino]-N-(6-oxo-5H-phenanthridin-2-yl)propanamide dihydrochloride

tert-Butyl *N*-[6-[methyl-[3-oxo-3-[(6-oxo-5*H*-phenanthridin-2-yl)amino]propyl]amino]hexyl]carbamate (110 mg, 0.22 mmol, 1 equiv) and HCl in EtOAc (3 mL, 4.5 mmol, 20.2 equiv) were combined and stirred overnight at 25°C. The reaction mixture was concentrated

to afford the title compound (99 mg, 0.22 mmol, 95% yield) as a light yellow solid. LC-MS: $[M+H]^+$ 395.3.

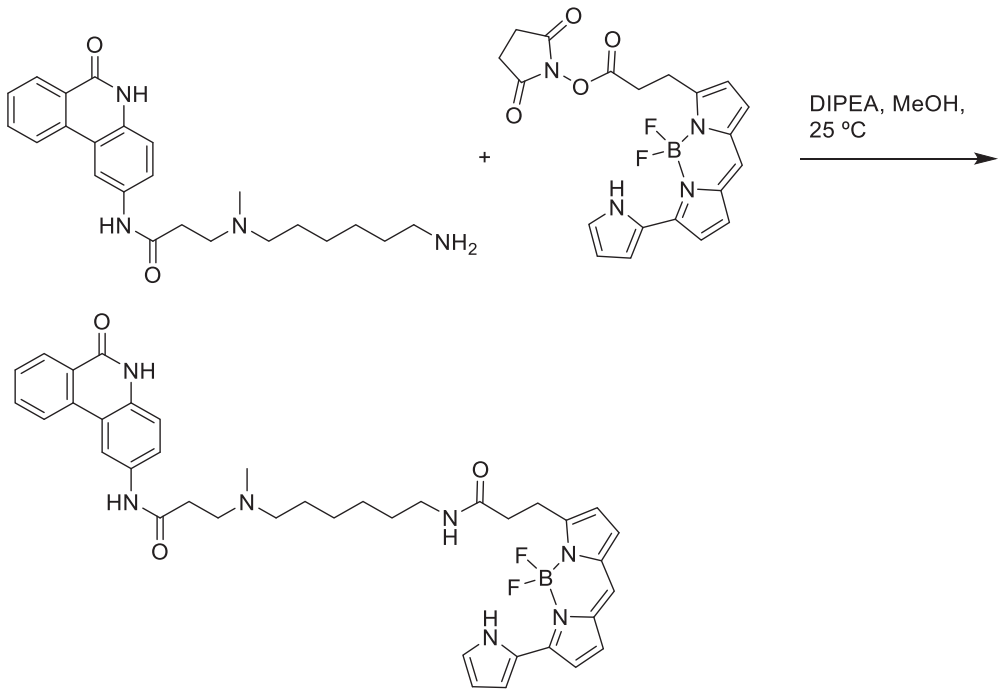

3-(5,5-difluoro-7-(1H-pyrrol-2-yl)-5H-5λ⁴,6λ⁴-dipyrrolo[1,2-c:2',1'-f][1,3,2]diazaborinin-3-yl)-N-(6-(methyl(3-oxo-3-((6-oxo-5,6-dihydrophenanthridin-2-yl)amino)propyl)amino)hexyl)propanamide

To a solution of 3-[6-aminohexyl(methyl)amino]-*N*-(6-oxo-5H-phenanthridin-2-yl)propenamide, 2,2,2-trifluoroacetic acid (12 mg, 0.02 mmol, 1 equiv) in DCM (2 mL) and MeOH (2 mL) was added DIPEA (0.08 mL, 0.47 mmol, 20 equiv). The mixture was stirred at 25°C for 5 min, and NanoBRET 590SE (10 mg, 0.02 mmol, 1 equiv) was added. The reaction mixture was covered with foil to avoid exposure to light and stirred at 25°C for 1 h. The resulting mixture was concentrated under vacuum. The crude product was directly purified by reverse-phase chromatography eluting with ACN/water (10% to 100%) and then ACN/water (20% to 100%, 0.1% TFA) to give ~10 mg crude product, which was further purified by prep-HPLC (ACN/water, 0.1% TFA) to give the title compound (5 mg, 0.006 mmol, 26% yield) as a blue-purple solid. LC-MS: $[M+H]^+$ 706.3. ^{1}H NMR (400 MHz, CD_3OD) δ 10.70 (s, 1H), 8.65 (d, J =1.6 Hz, 1H), 8.41 (d, J = 8.0 Hz, 1H), 8.30 (d, J = 8.0 Hz, 1H), 7.83 (t, J = 7.6 Hz, 1H), 7.69 – 7.56 (m, 2H), 7.31 (d, J = 8.8 Hz, 1H), 7.21 – 7.11 (m, 4H), 6.97 (d, J = 4.4 Hz, 1H), 6.89 (d, J = 4.0 Hz, 1H), 6.37 – 6.27 (m, 2H), 3.70 -3.62 (m, 1H), 3.40 - 3.35 (m, 1H), 3.29 – 3.09 (m, 6H), 2.97- 2.93 (m, 2H), 2.91 (s, 3H), 2.62 (t, J = 7.6 Hz, 2H), 1.85 – 1.77 (m, 2H), 1.57 - 1.53 (m, 2H), 1.50 - 1.38 (m, 4H).

RBN012337 (example 543A in (Vasbinder et al., 2019)) and RBN013293 (example 390 in (Schenkel et al., 2019)) were synthesized as previously described.

QUANTIFICATION AND STATISICAL ANALYSIS

Data Analysis for In Vitro Active Site Probe Displacement TR-FRET Assays

The TR-FRET was calculated using the following equation:

$$TRF = \frac{emission\ 665\ nM}{emission\ 615\ nM}$$

Data Analysis for Cellular Active Site Probe Displacement NanoBRET Assays

The BRET ratio was calculated using the following equation:

$$BRET\ ratio = \frac{Emission\ at\ 610\ nm}{Luminescence}$$

% Inhibition

The % inhibition for all assays was calculated as shown below:

$$\%\ inhibition\ = 100 \times \frac{signal_{cmpd} - signal_{min}}{signal_{max} - signal_{min}}$$

where $signal_{cmpd}$ is the assay signal from the compound treated well, $signal_{min}$ is the assay signal from the positive control well and $signal_{max}$ is the assay signal from the DMSO-treated negative control well.

IC_{50} Curve Fitting

The % inhibition values were plotted as a function of compound concentration and the following 4-parameter fit was applied to derive the IC_{50} values:

$$Y = Bottom + \frac{(Top - Bottom)}{1 + \left(\frac{X}{IC_{50}}\right)^{Hill\ Coefficient}}$$

Typically, the 4-parameters were allowed to float, however in some cases the bottom or top of the curves were fixed at 0% or 100% respectively.

Pass/Fail Criteria for Screening Plates

Plates were failed if the Z' (Zhang et al., 1999) was below 0.5, as well as if the IC_{50} value for a reference inhibitor included on each plate did not register to within 3-fold of its historical averaged IC_{50}.